A Static Modeling and Evaluation Framework for Soft Continuum Robots With Reinforced Chambers

Jialei Shi, Hanyu Jin, *Student Member, IEEE*, Wenlong Gaozhang, *Member, IEEE*, Ge Shi, *Member, IEEE*, Sara-Adela Abad, *Member, IEEE*, and Helge A. Wurdemann, *Member, IEEE*

***Abstract*—Elastomer-based soft manipulators with fibre-reinforced chambers, represent a prevalent design paradigm in soft robotics. These robots incorporate multiple actuation chambers, enabling elongation and bending motions. However, the inherent compliance of materials and the pressurized chambers inevitably introduce significant nonlinearity to these robots. Moreover, design of such robots often relies on a trial-and-error approach. Consequently, a comprehensive robot prototyping framework is of paramount importance. To achieve this, we present a static modeling, design and evaluation framework for soft robots with densely reinforced chambers (i.e., the angle between the reinforcement fibre and the axial direction of soft robots is 90°). We first propose a static analytical modeling framework to achieve both the forward kinematics and the tip force generation modeling. This modeling framework accommodates the effects of pressurized chambers and (non)linear material behaviors. Furthermore, our design and evaluation framework incorporates an open-accessible simulation toolbox with a user-friendly graphical interface, along with a physical evaluation platform. The entire framework is validated by eight kinds of manipulators with varying diameters and lengths. Meanwhile, the nonlinearity introduced by geometrical deformation resulting from the elongation, the pressurized actuation chambers (i.e., the chamber stiffening effect), and material hyperelasticity are investigated. Results also enable informed decision-making on design specifications prior to robot fabrication.**

***Index Terms*—Fibre-reinforced soft robots, fluidic elastomer actuators (FEAs), interaction force, statics and kinematics model.**

Received 24 July 2025; accepted 14 October 2025. Date of publication 28 October 2025; date of current version 17 November 2025. This work was supported in part by the Springboard Award of the Academy of Medical Sciences under Grant SBF003-1109, in part by the Engineering and Physical Sciences Research Council under Grant EP/R037795/1, Grant EP/S014039/1, and Grant EP/V01062X/1, and in part by the UCL Dean's Prize, and UCL Mechanical Engineering. This article was recommended for publication by Associate Editor F. Alambeigi and Editor H. Zhao upon evaluation of the reviewers' comments. *(Corresponding author: Helge A. Wurdemann.)*

Jialei Shi is with the Department of Mechanical Engineering, University College London, WC1E 6BT London, U.K., and also with the Hamlyn Centre for Robotic Surgery, Department of Mechanical Engineering, Imperial College London, SW7 2AZ London, U.K. (e-mail: j.shi@imperial.ac.uk).

Hanyu Jin is with the Department of Mechanical Engineering, Carnegie Mellon University, Pittsburgh, PA 15251-7525 USA (e-mail: hanyujin@andrew.cmu.edu).

Wenlong Gaozhang and Helge A. Wurdemann are with the Department of Mechanical Engineering, University College London, WC1E 6BT London, U.K. (e-mail: h.wurdemann@ucl.ac.uk).

Ge Shi is with the Department of Mechanical Engineering, University College London, WC1E 6BT London, U.K., and also with Robotics and Autonomous Systems Group, CSIRO, Pullenvale, QLD 4069, Australia (e-mail: ge.shi@csiro.au).

Sara-Adela Abad is with the Department of Mechanical Engineering, University College London, WC1E 6BT London, U.K., and also with the Universidad Nacional de Loja, Loja 110103, Ecuador.

This article has supplementary downloadable material available at https://doi.org/10.1109/TRO.2025.3626601, provided by the authors.

Digital Object Identifier 10.1109/TRO.2025.3626601

NOMENCLATURE

Abbreviation	*Description*
FEAs	Fluidic elastomer actuators.
M $*$ S#	#th step in the fabrication method $*$.
D $*$ L#	Robot label, $*$ and # denote the outermost diameter of robots and the length of the chamber, respectively.
LM model	Linear material model.
NH model	Neo-Hookean model.
MR model	Mooney–Rivlin model.
RMSE	Root mean square error.
MAPE	Mean absolute percentage error.
ODEs	Ordinary differential equations.
GUI	Graphical user interface.

Symbol	*Description*
$\hat{(\cdot)}$ or $(\cdot)^\wedge$	Mapping from $\mathbb{R}^3$ to $\mathfrak{so}(3)$, or from $\mathbb{R}^6$ to $\mathfrak{se}(3)$.
$(\cdot)(s)$	Variable has a function of the arc length variable s.
$(\cdot)_{x\|y\|z}$	x, y, or z Component of a variable.
$(\cdot)_s$	$\partial(\cdot)/\partial s$ Derivation of a variable with the arc length s.
$(\cdot)_{,0}$ or $(\cdot)_0$	Initial value of a variable.
$\Delta(\cdot)$	Variation of a variable.
$\|\| \cdot \|\|$	Euclidean norm of a variable.
L_0, L	Original and elongated length of the robot.
L_c^i	Length of the ith fibre-reinforced chamber.
D_r, r_{ro}	Diameter and radius of the robot.
D_i, r_{ri}	Diameter and radius of the central channel of the robot.
$D_{\text{cp}}, r_{\text{cp}}$	Diameter and radius of the chamber position of the robot.
D_c, r_{ci}	Diameter and radius of the actuation chamber.
r_{co}	Radius of the reinforced layer, with $r_{\text{co}} = r_{\text{ci}} + \delta_c$.
d^i	$\in \mathbb{R}^3$ Position vector of the ith chamber in the body frame.
δ_c	Wall thickness of the chamber.
δ_r	Thickness between the central channel and reinforced layer.
δ_s	Threshold value of the minimum silicone thickness.
α_1, α_2	Angle between two adjacent chamber and chamber pair.

$\lambda_1, \lambda_2, \lambda_3$	Principle material stretch ratios.
ϵ_1	Longitudinal strain.
E_l	Linearized 100% Young's Modulus, for the LM model.
E_t	Tangent modulus, for hyperelastic models.
G	Shear modulus for the silicone materials.
E_{P_e}, E_{P_b}	Elongation and bending modulus of the chamber stiffening.
I_1, I_2	First or second invariant in the hyperelastic model.
$\sigma_{1,e}, \sigma_{1,t}$	Longitudinal engineering and principal Cauchy (true) stress.
Π	Strain density function.
A, A_c	Area of the cross section of the robot and actuation chamber.
F_P	Force generated by pressurization in the body frame.
F_b	Blocked force at the tip position.
H_p	Contact point of the blocked point.
h	Horizontal distance between H_p and the origin.
k_b, k_e	Bending and elongation stiffness of the pressurized chambers.
F_{λ_1}	Force generated by stretch deformation of the material.
$R(s)$	$\in \mathbb{R}^{3\times3}$ Rotation matrix along the robot.
$p(s)$	$\in \mathbb{R}^3$ Translation vector along the robot.
c	$\in \mathbb{R}^{6\times6}$ Compliance density matrix $c = \text{diag}[c_{se}, c_{bt}]$.
c_{se}	$\in \mathbb{R}^{3\times3}$ Compliance density matrix for shear and elongation.
c_{bt}	$\in \mathbb{R}^{3\times3}$ Compliance density matrix for bending and torsion.
$v(s)$	$\in \mathbb{R}^3$ Local strain vector.
$u(s)$	$\in \mathbb{R}^3$ Local bending curvature vector.
$n(s)$	$\in \mathbb{R}^3$ Internal force along the rod.
$m(s)$	$\in \mathbb{R}^3$ Internal moment along the rod.
$f_e(s)$	$\in \mathbb{R}^3$ Distributed external force per unit s.
$m_e(s)$	$\in \mathbb{R}^3$ External moment per unit s.
$f_g(s)$	$\in \mathbb{R}^3$ Distributed gravitational force per unit s.
$f_P(s)$	$\in \mathbb{R}^3$ Distributed force from pressurization per unit s.
$m_P(s)$	$\in \mathbb{R}^3$ Distributed moment from pressurization per unit s.
J_z, I_x, I_y	(Polar) second moment of area about the z-, x-, and y-axes.
P^i	Pressure in the ith actuation chamber.
μ_i, β_i	Parameters for the NH and Ogden models.
C_{10}, C_{01}	Parameters for the MR and Yeoh models.
$(L_c^i)_{p^i\|F_b}$	Chamber lengths in the free and constrained space.
$e_{n\|m\|l\|h}$	Errors of the boundary conditions.
$W_{n\|m\|l\|h}$	Weight factors of the boundary conditions.

I. Introduction

THE inherent compliance of soft material robots results in high flexibility and adaptability of these systems, which is advantageous for manoeuvring in uncertain environments [1], [2], achieving safe robot-environment interactions [3], [4] and enabling dexterous motions [5], [6]. To construct soft robots, elastomers with various shore hardness ranges are typically used [7], [8]. Within this context, FEAs actuated by pressurized fluids are prevailing [9]. Essentially, multiple actuation chambers are created, and the entrapped fluids force the robot to produce strains. Consequently, the nonuniform strains make the robot to have elongation or (uni)directional bending motions [10].

A fabrication framework of the FEAs was summarized in [11], which elaborated different robot morphology, comprising the ribbed, cylindrical, and pleated design. For these FEAs, the radial expansion of the actuated chambers, i.e., the ballooning effect, is commonly observed resulting from the high deformability of soft elastomers. This ballooning effect might be advantageous, such as operating robots with a lower actuation pressure [12] and anchoring the robot [13]. Conversely, the ballooning effect may also have drawbacks, e.g., limiting the maximum motion ranges [14] and resulting in irregular kinematic behaviors [15], leading to potential interference between actuation chambers and embedded sensors [16]. To prevent soft robots from ballooning, fibre-reinforced design is proposed. The concept is to wrap in-extensible fibre or sheath around the FEAs to restrain the radial expansion while allowing longitudinal elongation. This design mitigates the ballooning effect and avoid potential chamber interferences of robots.

A. Related Work

The pioneering work of fibre-reinforced FEAs can date back to the late 80s, when the microactuators were proposed for manipulation and locomotion tasks [17]. These microactuators comprised fibre-reinforced rubber and three actuation chambers of a sector shape. Over time, this principle has developed and evolved in various fields. Specifically, the reinforcement can be achieved by two approaches, body reinforcement and chamber reinforcement. A typical example using the body reinforcement is the original design of the stiffness controllable flexible and learnable manipulator for surgical operations (STIFF-FLOP) manipulator in [18], aiming for minimally invasive surgery (MIS). In this design, three semicircular actuation chambers and one central stiffening chamber were integrated. A crimped sheath was employed externally to confine the robot's radial expansion. In addition, in-extensible fibres can be used to impose radial constraints. This enables the creation of miniaturized robots (with a diameter of 6 mm) featuring a central working channel [19], bending actuators with various cross-sectional geometries [20], [21], [22] and soft grippers [23], [24]. While body reinforcement can alleviate the ballooning effect, the actuation chambers may still undergo expansion, potentially leading to unwanted interference between actuation chambers and other working channels. To address this issue, the chamber reinforcement was explored. An improved fabrication process for the STIFF-FLOP manipulator was presented in [15]. In this approach, each individually reinforced

chamber effectively limits the expansion of actuation chambers and enhances robot's motion ranges. Miniaturized manipulators, e.g., with a diameter of 14.5 mm, were then produced [25].

Broadly speaking, leading modeling techniques for soft robots encompass numerical, analytical and data-driven approaches [26]. The finite element method (FEM) is a numerical approach, which describes the robot geometries by mesh comprising a set of nodes together with the information about neighboring nodes [27], [28]. However, the FEM might be computationally demanding as it relies on large numbers of nodes. To reduce the geometrical complexity, analytical approaches have been developed. For instance, the curvature along the backbone of soft robots can be assumed to be constant, resulting in the static or dynamic piece-wise constant curvature (PCC) models [29], [30]. On the other hand, variable curvature models have been proposed, for instance, the Cosserat rod model [31], [32], [33], the piece-wise constant or linear strain models [34], [35]. In scenarios where there are uncertainties in the model, data-driven methods, e.g., model-based estimation [36], parametric fitting [37], and learning approaches [38], can be considered.

Based on these modeling advances, soft robots with fibre reinforcement can be described. Essentially, reinforcing the robots using threads shares the similarity with the Mckibben muscles [39]. The relationship between the fibre angle and actuator responses was investigated using FEM in [40], and a mechanical programming method was proposed to achieve a versatile locomotion. Likewise, an analytical model was explored in [41], wherein the optimization can be implemented to determine design parameters, such as the fibre angle, to replicate a comparable kinematic trajectory of the fingers. Connolly et al. [40] also highlighted that when the fibre is densely reinforced, i.e., the fibre is approximately perpendicular to the longitudinal axis, the maximum elongation capability is attained. The dense reinforcement assumption also brings convenience for modeling, as it allows the circumference of the reinforced layer to be considered as invariant [42]. In addition, Polygerinos et al. [21] proposed an analytical model employing the Neo-Hookean material model to predict the bending angle and blocked force of a unidirectional bending actuator. Sadati et al. [43] proposed a dynamics modeling methodology for hybrid rigid-continuum systems and demonstrated its application using the STIFF-FLOP manipulators, provided the chambers were densely reinforced. Renda et al. [44] proposed a screw-based forward kinematics modeling method using the Cosserat rod theory, utilizing the assumption of a linear material behavior. In addition to establish analytical kinematics or dynamics models directly, data-driven methods have been explored. In [23], the relationship between the actuation pressure and chamber length was experimentally identified and used to derive the forward and inverse kinematics, based on the PCC model. Huang et al. [45] developed a model to describe and parameterize the kinematics and stiffness characterizations of soft parallel robots, with each leg fibre-reinforced. In [43], [44], and [45], a linear material behavior was assumed with a constant Young's Modulus. However, nonlinearity is observed with the increase of the strains [15], [21], and the pressurization could also influence the stiffness properties of soft robots [46], [47].

In addition to addressing the challenges of designing and modeling robots separately, significant efforts have been made to develop comprehensive and efficient tools and methods for prototyping, evaluating, and controlling robots. This includes the development of both physical platforms and software toolboxes [48], [48]. An experimental platform was proposed in [49] to achieve multiple degrees of freedom force characterizations of fibre-reinforced bending actuators. Several MATLAB toolboxes, such as SoRoSim [50], Sorotoki [51], and SPADA [52], have been developed based on geometric variable strain models or FEM. These toolboxes facilitate the modeling, simulation and analysis of soft or hybrid rigid-soft robotic systems. In addition, the open-source Simulation Open Framework Architecture [27], has flourished in the soft robotics community, which establishes an FEM-based simulation and control framework with abundant and versatile plugins. Beyond tool developments, there has been exploration into general design, modeling, and development methodologies to streamline the prototyping of soft robots [53], [54]. For instance, a statics modeling framework is proposed in [55], to depict free bending, block force, and deflection upon block force for fibre-reinforced actuators, while these actuators can only achieve planar bending motions.

In summary, soft robots with a fibre reinforcement have been investigated for a wide spectrum of applications and described using various modeling techniques. As such, the robot modeling, design and evaluation lay the foundation for the prototyping and developing of fibre-reinforced robots. Particularly, this work focuses on soft robots with dense fibre-reinforced, extending actuation chambers with a central working channel. These robots offer several important advantages. First, these extending actuators can achieve much higher stretch ratios, exceeding 50% [21], [22], which enables larger bending curvatures compared to fibre-reinforced contracting actuators. For instance, the theoretical maximum contraction ratio for a McKibben muscle is 36.3%, and typical values range from 20%–30% [56]. Second, full fibre reinforced-chambers eliminate the ballooning effect and preserve the cross-sectional geometry during pressurization [33], ensuring that tools inserted into the central channel are not compressed. Third, because the reinforced chambers do not expand radially, the required input fluid is reduced, actuator response becomes more linear, and overall system durability is improved [57].

Specifically for these soft manipulators, there remains a need for a modeling and evaluation framework capable of assessing key design parameters prior to robot prototyping, such as robot dimensions and material choices, to determine their suitability for potential applications. Such a framework would support more informed decision-making in the early design stage and help reduce overall prototyping time. In addition, the nonlinearity introduced by the compliant materials and the pressurized chambers still needs to be investigated, especially considering non-negligible longitudinal deformation.

B. Contributions and Outline

To enable informed decision-making on design specifications for the development of fibre-reinforced soft robots, this article

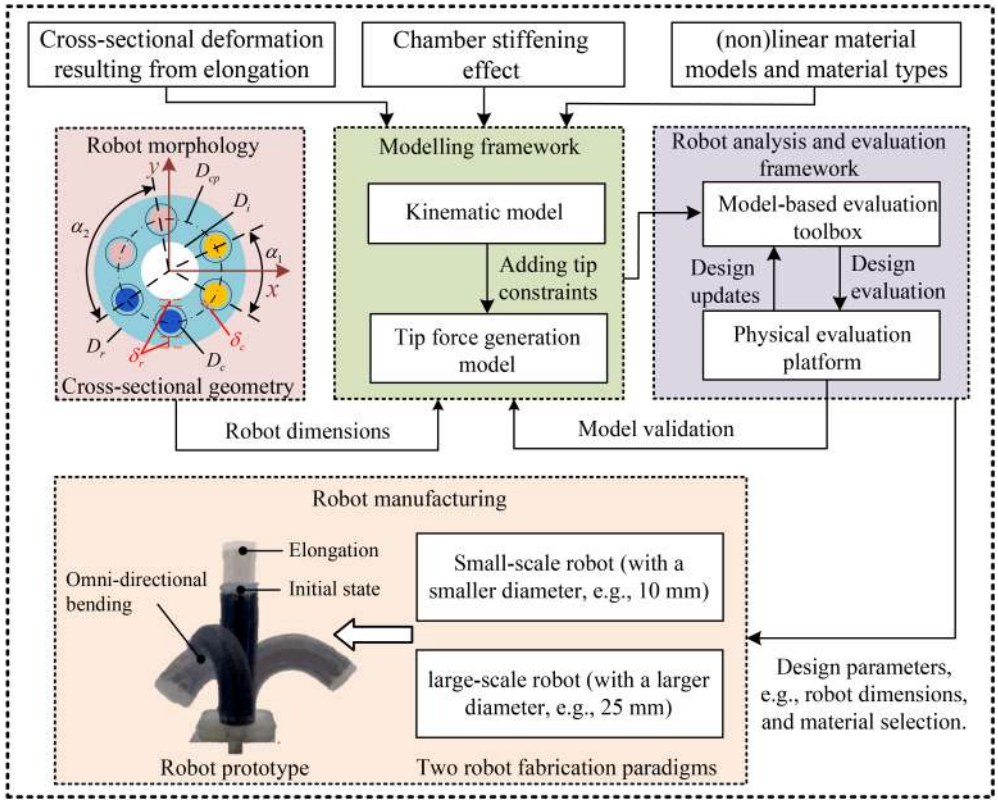

Fig. 1. Proposed static modeling and evaluation framework for soft robots with densely reinforced chambers. The angle between the reinforcement fibre and the axial direction can be approximated as 90°. The variables are explained in the Nomenclature.

proposes a static modeling and evaluation framework to evaluate two key robot performances, i.e., forward kinematics and tip force generation capability, for soft robotic manipulators with multiple reinforced chambers, based on the robot geometric design and soft material properties (see Fig. 1). We first present the analytical statics modeling framework, including the forward kinematics and the tip force generation models. The modeling framework can investigate different material models, e.g., linear material model or nonlinear hyperelastic models (Neo-Hookean model, Mooney–Rivilin model, Yeoh model, and Ogden model) and incorporate the influences of the pressurization chambers. The robot evaluation framework is then proposed by encapsulating the proposed analytical models into an open-accessible simulation toolbox with GUI to assess soft robots based on the design parameters. Access to the Github toolbox is available upon request by completing the form at https://forms.gle/DJNQDFSh3SVtjVKv6. Meanwhile, a physical platform is presented to achieve experimental evaluations of soft robots. We then validate our framework via a set of soft manipulators with eight different dimensions (outer diameters of 25 mm, 20 mm, 15 mm, and 10 mm, lengths of 40 mm and 60 mm), from the robot fabrication to the simulation and experiment. The main contributions of this work are as follows.

1) A comprehensive static modeling and evaluation framework is proposed to assess two key performances of soft robots featuring reinforced chambers, i.e., the forward kinematics and the tip force generation (see Fig. 1). The entire framework encompasses analytical models (see Section II), open-access simulation software (see Section III-A), and experimental evaluation platform (see Section III-B). The framework can be used to determine key robot design parameters prior to robot prototyping for specific applications (see Section V).
2) The analytical models in the framework are versatile, incorporating nonlinearity resulting from compliant materials, various material models, material types (see Section II-E), and impacts of the pressurized chambers (see Section II-C).
3) The efficacy of the framework is extensively validated through a combination of simulations and experiments involving eight types of robots (see Section IV). All experiments accommodate a wide spectrum of robot design parameters and offer a valuable characterization dataset for these robots.

The rest of this article is organized as follows. Section II presents the analytical statics modeling framework, including the forward kinematics and force-generation models using the Cosserat rod theory. Section III describes the robot evaluation framework, including a simulation toolbox built on the modeling framework established in Section II and a physical platform for experimental characterization of soft robots. The validation of the framework is then presented in Section IV via simulations and experiments, to characterize performances of soft robots with different dimensions and further demonstrate the efficacy of the framework. Section V showcases using the framework to design and evaluate a soft robotic laparoscope. The corresponding

discussions and reflections are presented in Section VI. Finally, Section VII concludes this article.

II. Analytical Statics Modeling Framework

This section details the analytical statics modeling framework for soft robots with densely reinforced chambers (i.e., the angle between the reinforcement fibre and the axial direction of soft robots is approximately 90°). The robot morphology is first presented. Next, the forward kinematics model is established based on the Cosserat rod model, considering the chamber stiffening effect and cross-sectional deformation. To further describe the robots' force capability, a planar tip force generation model is established considering length constraints of pressurized chambers. The modeling framework is finalized by incorporating linear or hyperelastic material models. The numerical implementations conclude this section.

A. Robot Morphology

As highlighted in Section I-A, the morphology of the soft robots in this article inspired by the STIFF-FLOP design [15] and comprises densely reinforced chambers. Characteristics of this design is summarized as follows.

1) Pneumatic-driven chambers are distributed around a central working channel to achieve both elongation and omni-directional bending motions (see Fig. 1).
2) Each chamber is individually reinforced by in-extensible fibres to constrain the radial expansion.
3) The fibre is densely reinforced, with the fibre angle *w.r.t* the axial direction of 90° to maximize the elongation capability [40].

The cross-sectional geometries of the robots are shown in Fig. 1. A central working channel is reserved for feeding through appendages, and six pneumatic-driven actuation chambers are designed. In this article, every two adjacent chambers are actuated as one pair. To have a feasible fabrication, the constraints of the cross-sectional dimension (see Fig. 1) are

$$\begin{aligned} &D_i + 4(\delta_c + \delta_r) + 2D_c = D_r \\ &\text{s.t.} \quad \delta_c + \delta_r \geq \delta_s \end{aligned} \tag{1}$$

where D_i, D_r, and D_c are the diameter of the robot, chamber, and central channel, respectively. δ_c is the wall thickness of the chamber, δ_r is the silicone thickness between the central channel and the reinforced layer. δ_s is the threshold of the minimum silicone thickness to guarantee the fabrication is feasible. δ_s is empirically determined as 0.8–1 mm.

B. Forward Kinematics Model

Considering that the stretch ratio of the robots can be larger than 1.5, the deformation of the cross-sectional geometry is non-negligible when the robot elongates. Here, the kinematics model is built on the static Cosserat rod model [31], considering the cross-sectional deformation and longitudinal elongation. In general, by differentiating with the arc length of the backbone

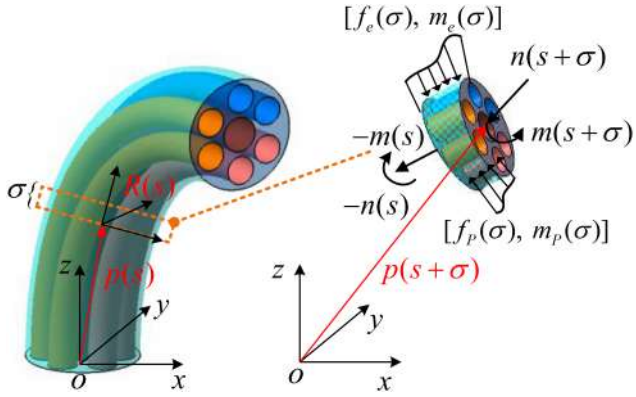

Fig. 2. Illustration of the force and moment equilibrium for the robot. The length of the element is σ. Apart from the external distributed force $f_e(s)$ and moment $m_e(s)$, the pressurization also introduces the distributed force $f_P(s)$ and moment $m_P(s)$ along the arc s.

s, the robot kinematics can be described via a set of ODEs

$$\begin{cases} p_s(s) = R(s)v(s) \\ R_s(s) = R(s)\hat{u}(s) \\ n_s(s) = -f_e(s) + f_P(s) \\ m_s(s) = -\hat{p}_s(s)n(s) - m_e(s) + m_P(s) \end{cases} \tag{2}$$

where $p_s(s)$ is the derivative of the position vector $p(s)$, $R_s(s)$ is the derivative of the rotation matrix $R(s)$. $v(s)$ and $u(s)$ are the local strain and the curvature expressed in the body frame, respectively. $n_s(s)$ and $m_s(s)$ are the derivative of the internal force $n(s)$ and moment $m(s)$. $f_e(s)$ and $m_e(s)$ are the distributed external force and moment. $\hat{(\cdot)}$ is the mapping from $\mathbb{R}^3$ to $\mathfrak{so}(3)$. $f_P(s)$ and $m_P(s)$ are the distributed force and moment resulting from the pressurization. The force equilibrium of an infinitesimal element σ (see Fig. 2) is

$$\begin{aligned} &\int_s^{s+\sigma} f_e(s)\mathrm{d}\sigma + n(s+\sigma) - n(s) \\ &- \sum_{i=1}^{6} [P^i A_c (R(s+\sigma) - R(s))e_3] = 0. \end{aligned} \tag{3}$$

σ is the length of the element. P^i is the pressure in the ith chamber, A_c is the chamber area. $e_3 = [0,0,1]^T$ is a unit vector. Similarly, the moment equilibrium (see Fig. 2) is

$$\begin{aligned} &m(s+\sigma) - m(s) + p(s+\sigma) \times n(s+\sigma) - p(s) \times n(s) \\ &+ \int_s^{s+\sigma} [m_e(s) + p(s) \times f_e(s)]\mathrm{d}\sigma \\ &- \sum_{i=1}^{6} \{[p(s+\sigma) + R(s+\sigma)d^i] \times (P^i A_c R(s+\sigma)e_3) \\ &- [p(s) + R(s)d^i] \times (P^i A_c R(s)e_3)\} = 0. \end{aligned} \tag{4}$$

By differentiating (3) and (4), $f_P(s)$ and $m_P(s)$ in (2) are

$$\begin{cases} f_P(s) = & \sum_{i=1}^{6}[P^i A_c R_s(s) e_3] \\ m_P(s) = & \sum_{i=1}^{6} P^i A_c R(s)[(v(s) + \hat{u}(s) d^i) \times e_3 \\ & + \hat{d^i} \hat{u}(s) e_3)] \end{cases} \tag{5}$$

where d^i is the position vector from the centre of the robot to the centre of the ith chamber in the body frame. The resulting force from the pressurization in the body frame is

$$F_P = \sum_{i=1}^{6} P^i A_c = \sum_{i=1}^{6} P^i \pi r_{ci}^2 \tag{6}$$

where r_{ci} is the radius of the actuation chamber. The local strain $v(s)$ vector can be separated as

$$v(s) = v(s)_P + v(s)_e \tag{7}$$

where $v(s)_P$ results from the pressurization and $v(s)_e$ results from external forces containing shear strains. Considering the pressure is always perpendicular to the cross-section of the robot, so the pressurization generates no shear strains [59]. As such, $v(s)_P$ equals $\lambda_1 e_3$. Therefore, the constitutive model of an elongated element (with a longitudinal stretch ratio of λ_1) can be rewritten as

$$\begin{cases} v(s) = c_{se}[R(s)^T n(s) - F_P e_3] + e_3 \\ u(s) = c_{bt} R(s)^T m(s) \end{cases} \tag{8}$$

where $c = \text{diag}[c_{se}, c_{bt}]$, is the compliance density matrix. $c_{se} = \text{diag}[GA, GA, EA]^{-1}$ contains the shear and elongation compliance. $c_{bt} = \text{diag}[EI_x, EI_y, GJ_z]^{-1}$ contains the bending and torsion compliance. G is the shear modulus. I_x, I_y, and J_z are the second moment of area around the x-, y-, and z-axis. Please note that considering the elongation and shrinking deformation of the cross-section, the density matrix c depends on the value of λ_1. The derivation of c can be found in Section S.V. of the Supplementary Material.

To solve (2), tip boundary conditions need to be satisfied. Errors of the boundary conditions can be defined as

$$\begin{cases} e_n = F_e(L) + R(L) \sum_{i=1}^{6} A_c P^i e_3 - n(L) \\ e_m = M_e(L) + R(L) \sum_{i=1}^{6} (d^i \times A_c P^i e_3) - m(L) \end{cases} \tag{9}$$

where L is the robot length, $n(L)$ and $m(L)$ are the integrated force and moment at the tip position, $F_e(L)$ and $M_e(L)$ are the applied external tip force and moment. Combining (2)–(9), (2) can be solved using the shooting method, with the error set of $e = [e_n, e_m]$ and the integration interval of L. The guess variables $g(0)$ for the initial conditions are $[n(0), m(0)]$.

C. Stiffening Effect of Pressurized Chambers

It is observed that the bending or elongation exhibit nonlinearity under a higher pressure [22]. This could be modeled by considering the bending and elongation stiffness resulting from pressurized chambers, which can be regarded as linearly increasing with the pressure [46], [60]. To further incorporate the influence of the pressurized chambers, the additional stiffening force F_c can be describe by

$$F_c = \sum_{i=1}^{6} F_c^i = \sum_{i=1}^{6} k_e P^i A_c (\lambda_1 - 1) \tag{10}$$

where F_c^i is the equivalent stiffening force of the ith chamber, with the elongation stiffness coefficient as k_e. To incorporate the chamber stiffening into the model, EA in (8) can be substituted by the equivalent $(EA)_{\text{eq}}$, which yields

$$(EA)_{eq} = EA + \sum_{i=1}^{6} (E_{P_e} A_c)^i = EA + k_e \sum_{i=1}^{6} P^i A_c. \tag{11}$$

$(E_{P_e} A_c)^i$ is the elongation stiffness of the ith pressurized chamber and dependent on the pressure, with an equivalent bending stiffness of k_b.

Furthermore, the pressurized chambers also increase the bending stiffness $EI_{x|y}$ in (8), which influences the bending curvature. Similarly, the equivalent $(EI_{x|y})_{\text{eq}}$ updates as

$$(EI_{x|y})_{\text{eq}} = EI_{x|y} + \sum_{i=1}^{6} (E_{P_b} I_{c_{x|y}})^i = EI_{x|y} + k_b \sum_{i=1}^{6} P^i I_{c_{x|y}}^i. \tag{12}$$

$(E_{P_b} I_{c_{x|y}})^i$ is the resulting bending stiffness of the ith pressurized chamber and pressure-dependent. The calculation of $I_{c_{x|y}}^i$ can be found in Section S.V. of the Supplementary Material.

D. Planar Tip Force Generation Model

The interaction force between the soft robots and environments is a deeply interested topic [61], [62]. For continuum robots, the actuation principles, e.g., tendons or pressurized chambers [63], [64], might have influences on robots' properties. As such, a planar tip force generation model is proposed in this section, considering the constraints resulting from the pressurized chambers.

Along with the ODEs in (2), the derivative of the length of the ith chamber with respect to the arc s, i.e., L_c^i, can be described using

$$L_s(s)_c^i = ||R(s) d^i + p(s)||_s = ||\hat{u}(s) d^i + v(s)|| \tag{13}$$

for the norm of rotation matrix $||R(s)|| = 1$.

By solving (2)–(9) and (13), the kinematics and all the chamber lengths in the free space (with no interaction between the robot and the environment) can be solved. When the robot contacts with the environment and the tip is constrained (as shown in Fig. 3), the blocked force F_b can be considered to drive the robot from the free-space shape (transparent green color) to the constrained shape (solid green colour). Considering the pressure in the chambers is actively controlled as invariant, pressurized chambers tend to deform instead of contracting in the constrained shape. As such, this constraint can be described by

$$e_L = \sum_{i=1}^{6} [(L_c^i)_{P^i} - (L_c^i)_{F_b}], \; P^i > 0. \tag{14}$$

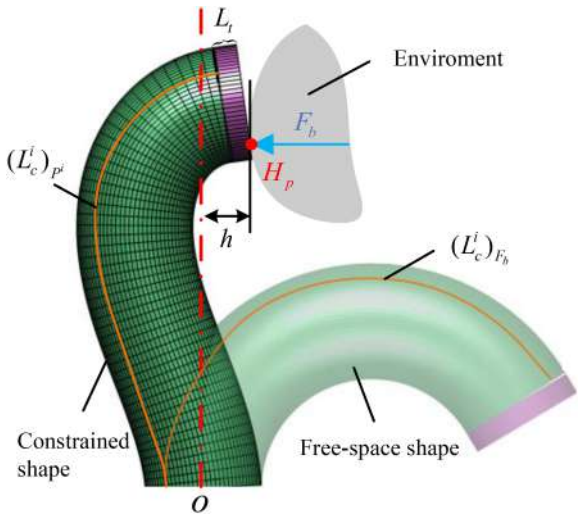

Fig. 3. Diagram of the robot-environment interaction. The transparent shape illustrates the robot deformation in the free-space; the solid shape shows the robot deformation subjected to a tip force F_b at point H_p due to the interaction with the environment. h is the horizontal offset distance between H_p and the origin point o. L_t is the length of the tip cap. $(L_c^i)_{P^i}$ and $(L_c^i)_{F_b}$ are the length of the ith pressurized chamber from the free-space shape and constrained shape, respectively.

$(L_c^i)_{P^i}$ and $(L_c^i)_{F_b}$ are the length of the ith pressurized chamber under the free-space and constrained shapes, respectively (see Fig. 3). e_L is the length difference of the pressurized chambers. Please note this length constraint is only activated for pressurized chambers, i.e., when $P^i > 0$.

The position constraints need to be considered to predict the blocked force F_b. As shown in Fig. 3, the horizontal displacement between the contact point H_p and the origin o is h. This constraint yields

$$e_h = H_p - h \tag{15}$$

where H_p is the position of the contact point in the horizontal direction and e_h is the position error.

F_b is considered as the external tip force and no external tip moment is applied. Constraints from the original boundary condition (9) become

$$\begin{cases} e_n = F_b + R(L)\sum_{i=1}^{6} A_c P^i e_3 - n(L) \\ e_m = R(L)\sum_{i=1}^{6}(d^i \times A_c P^i e_3) - m(L). \end{cases} \tag{16}$$

In summary, the new set of the ODEs including chamber lengths is

$$\begin{cases} p_s(s) = R(s)v(s) \\ R_s(s) = R(s)\hat{u}(s) \\ n_s(s) = -f_e(s) + f_P(s) \\ m_s(s) = -\hat{p}_s(s)n(s) - m_e(s) + m_P(s) \\ L_s(s)_c^i = ||\hat{u}(s)d^i + v(s)||. \end{cases} \tag{17}$$

Combining (14)–(17), the whole boundary conditions are $e = [e_n, e_m, e_L, e_h]$. For a better scaling of the shooting problem, weight coefficients are introduced, which yields

$$e = W_n e_n + W_m e_m + W_L e_L + W_h e_h \tag{18}$$

where W_n, W_m, W_L, and W_h are the weight coefficients. Please note that all the coefficients are larger than 1 in the implementation, e then could not be nullified. Such scaling technique results in a better solver convergence [63]. The guess variables now become $g(0) = [n(0), m(0), F_b]$, so the blocked force can be predicted using the shooting method.

E. Material Model

The forward kinematics and force-generation model both depend on the longitudinal stretch λ_1. To complete the modeling framework, the derivation of λ_1 is detailed using both linear and hyperelastic material models in this section.

1) Linear Material Model: The linearized 100% modulus E_l is commonly used to depict the tensile strength of silicone materials. The engineering axial stress $\sigma_{1,e}$ and axial stress ϵ_1 can be related using E_l, and the force balance yields

$$F_{\lambda_1} = A_0\sigma_{1,e} = A_0 E_l \epsilon_1 = A_0 E_l \frac{\Delta L}{L_0} \tag{19}$$

where F_{λ_1} is the force generated by stretch deformation of silicone materials. A_0 is the initial cross-section area, ΔL and L_0 are the variation and original robot length. The longitudinal stretch equals $\lambda_1 = 1 + \epsilon_1$. A linear strain-stress approximation can be applied when the strain is small, but it cannot capture the nonlinear hyper-elasticity when the strain increases.

2) Hyperelastic Material Model: Furthermore, hyperelastic models can be adopted, which are built upon the strain density function Π using strain invariants. The first invariant $I_1 = \lambda_1^2 + \lambda_2^2 + \lambda_3^2$, where the axial, circumferential, and radial stretch ratio is λ_1, λ_2, and λ_3, respectively. The second invariant $I_2 = \lambda_1^2\lambda_2^2 + \lambda_2^2\lambda_3^2 + \lambda_1^2\lambda_3^2$. The silicone material can be regarded as incompressible ($\lambda_1\lambda_2\lambda_3 = 1$). The principal Cauchy stress $\sigma_{i,t}$ under a uni-axial stretch condition equals

$$\begin{aligned} &\sigma_{i,t} = \lambda_i \frac{\partial \Pi}{\partial \lambda_i} - p_h = \lambda_i \sigma_{i,e} \\ &\text{s.t.} \quad \sigma_{2,t} = \sigma_{3,t} = 0,\ \lambda_2 = \lambda_3 = \frac{1}{\sqrt{\lambda_1}} \end{aligned} \tag{20}$$

where p_h represents the hydrostatic pressure serving as the constraint, due to the incompressiblility of materials. Based on the construction of the energy function Π, different hyperelastic models can be established. The axial engineering stress $\sigma_{1,e}$ is derived by solving (20) and summarized in Table I. Four models, the Neo-Hookean (NH) model, the Mooney–Rivlin (MR) model , the Yeoh model, and the Ogden model, are investigated with λ_1 up to 2, for the elongation ratio of the robots is less than 100%. To identify model parameters for commonly used silicone materials, such as Ecoflex 00-10 to 00-50, tensile test is conducted and the maximum stretch λ_1 is set as 2. The details of the strain-stretch curve and identified material parameters are in Table I.

Similar to (19), the force from hyperelastic models is

$$F_{\lambda_1} = A\sigma_{1,t} = \frac{A_0}{\lambda_1}\sigma_{1,t} \tag{21}$$

where A is the deformed cross-section area (see Section S.V. of the Supplementary Material). Assuming the radius of the

TABLE I
ENGINEERING STRESS OF DIFFERENT MATERIAL MODELS UNDER THE UNI-AXIAL STRETCH TEST, WITH THE IDENTIFIED PARAMETERS

Model	Strain energy density function (II)	Engineering stress ($\sigma_{1,e}$ [MPa])
Neo-Hookean (NH) model	$\frac{\mu_0}{2}(I_1-3)$	$\mu_0(\lambda_1-\frac{1}{\lambda_1^2})$
Mooney-Rivlin (MR) model	$C_{10}(I_1-3)+C_{01}(I_2-3)+C_{20}(I_1-3)^2$	$2(\lambda_1-\frac{1}{\lambda_1^2})[C_{10}+2C_{20}(I_1-3)+\frac{C_{01}}{\lambda_1}]$
Yeoh model	$C_{10}(I_1-3)+C_{20}(I_1-3)^2$	$2(\lambda_1-\frac{1}{\lambda_1^2})[C_{10}+2C_{20}(I_1-3)]$
Ogden model	$\sum_{i=1}^{2}\frac{\mu_i}{\beta_i}(\lambda_1^{\beta_i}+2\lambda_1^{-\beta_i/2}-3)$	$\sum_{i=1}^{2}\mu_i(\lambda_1^{\beta_i-1}-\lambda_1^{-\beta_i/2-1})$

Silicone material	NH model	MR model	Yeoh model	Ogden model
Dragon Skin 10	$\mu_0=0.07980$	$C_{10}=0.01848, C_{20}=0.001657$ $C_{01}=0.02958$	$C_{10}=0.04112,$ $C_{20}=-0.0005151$	$\mu_1=1.413, \beta_1=0.1295$ $\mu_2=0.001185, \beta_2=6.215$
Ecoflex 00-50	$\mu_0=0.03091$	$C_{10}=0.00376, C_{20}=0.001047$ $C_{01}=0.01558$	$C_{10}=0.01569,$ $C_{20}=-9.767\times10^{-5}$	$\mu_1=-3.88\times10^{-5}, \beta_1=7.513$ $\mu_2=-0.01479, \beta_2=-5.983$
Ecoflex 00-30	$\mu_0=0.01971$	$C_{10}=0.003321, C_{20}=0.0004978$ $C_{01}=0.009057$	$C_{10}=0.01025,$ $C_{20}=-0.0001674$	$\mu_1=0.1186, \beta_1=0.3701$ $\mu_2=9.457\times10^{-5}, \beta_2=7.951$
Ecoflex 00-20	$\mu_0=0.01361$	$C_{10}=0.002731, C_{20}=0.0003398$ $C_{01}=0.00553$	$C_{10}=0.006964,$ $C_{20}=-6.619\times10^{-5}$	$\mu_1=0.01257, \beta_1=1.345$ $\mu_2=0.01078, \beta_2=1.349$
Ecoflex 00-10	$\mu_0=0.00964$	$C_{10}=-0.0009413, C_{20}=0.0005407$ $C_{01}=0.007575$	$C_{10}=0.004857,$ $C_{20}=-1.539\times10^{-5}$	$\mu_1=342.3, \beta_1=6.518\times10^{-5}$ $\mu_2=6.371\times10^{-5}, \beta_2=7.67$

* The unit of the parameters is MPa. The details of the fitting results of the stress-stretch curve can be found in Fig. S1 of the Supplementary Material.
* All samples cure at 60 °C for 30 minutes; dimensions are 12 × 3 × 50 mm; the stretching speed is set as 0.2 mm/s. Each test repeated three times.

reinforced layer r_{co} keeps constant after pressurization, so $r_{\text{co},0}=r_{\text{co}}$. The reinforced rubber volume keeps invariant, this yields

$$\pi(r_{\text{co},0}^2-r_{\text{ci},0}^2)L_{c,0}^i=\pi(r_{\text{co}}^2-r_{\text{ci}}^2)\lambda_1 L_{c,0}^i \tag{22}$$

so r_{ci} can be solved and depends on the pressurization. $r_{\text{ci},0}$ and $r_{\text{co},0}$ are the initial inner and outer radius.

The longitudinal stretch ratio λ_1 is derived by considering the force balance between the actuation force F_P, stiffening force F_c, and material stretch force F_{λ_1}, which yields

$$F_{\lambda_1}=F_P+F_c. \tag{23}$$

F_c should be excluded when forces resulting from the stiffening effect is not considered.

Combining (10), (21), and (23), λ_1 can be solved numerically based on hyperelastic models. Similarly, combining (10), (19), and (23), λ_1 can be solved using the linearized material model. Different from the linear material model, the modulus varies with the stretch ratio in hyperelastic models. As such, the tangent modulus E_t under the axial stretch ratio of λ_1 can be calculated by

$$E_t=\frac{\mathrm{d}\sigma_{1,t}}{\mathrm{d}\lambda_1}. \tag{24}$$

The compliance density matrix c can then be constructed using λ_1, the modulus E_l (for linear material model) or E_t (for hyperelastic model), and deformed cross-sectional geometries.

By now, the modeling framework is completed. λ_1 and the parameters of material models can be substituted to derive the kinematics model (see Section II-B) and tip force generation model (see Section II-D). This modeling framework can consider the cross-sectional deformation resulting from the elongation and incorporate various material models. It also can include the stiffening effect of the pressurized chambers (see Section II-C).

F. Numerical Implementation

The numerical implementation of the free-space kinematic modeling is in Algorithm 1, the variable state $y=[p,R,m,n,L_c^i]_{1\times24}$. The initial position vector $p(0)$ is $[0,0,0]$, $R(0)$ equals reshaping a 3×3 identity matrix to a 1×9 vector, $L(0)_c^i$ is a 6×1 zero vector. The initial guess $g(0)=[n(0),m(0)]$. Specifically, the stretch ratio λ_1 is derived by solving the force balance equation (23) using linear or hyperelastic material models. For hyperelastic models, the tangent modulus is derived from (24). Combining the deformed cross-sectional geometries (see Section S.V. of the Supplementary Material) and tangent modulus, the compliance density matrix c is obtained. Finally, by integrating (17) and satisfying the boundary condition (9), the free-space kinematics is solved.

Algorithm 1: Free-Space Kinematics.

Input: pressure P, the material model and parameters, robot dimensions.
Output: chamber lengths L_c^i in the free-space, position vector $p(s)$, rotation matrix $R(s)$.
Initialisation: cross-sectional geometries $A_0, I_{x,0}, I_{y,0}, J_{z,0}$, initial guess $g(0)$, convergence tolerance ϵ;
1: $\lambda_1, E_t \leftarrow$ solve (10), (21), (23) to get the stretch ratio;
2: $\lambda_1, E_l \leftarrow$ solve (10), (19), (23) to get the stretch ratio;
3: construct the compliance density matrix c, (11) and (12), considering the longitudinal stretch λ_1.
4: **while** $e \geq \epsilon$ **do**
5: $n(L), m(L) \leftarrow$ integrate (17) using $g(0)$ via the Fourth-order Runge-Kutta method, with $g(0)=[n(0),m(0)]$;
6: $e \leftarrow [e_n, e_m]$, evaluate errors from the boundary condition (9);
7: update $g(0)$ via the Levenberg–Marquardt method;
8: **end while**
9: **return** $(L_c^i)_{P^i}, p(s), R(s)$;

The implementation of the tip force generation model is summarized in Algorithm 2, the variable state y and its initial values are the same as Algorithm 1. Instead, the initial guess becomes $g(0)=[n(0),m(0),F_b]$ to include the blocked tip force F_b.

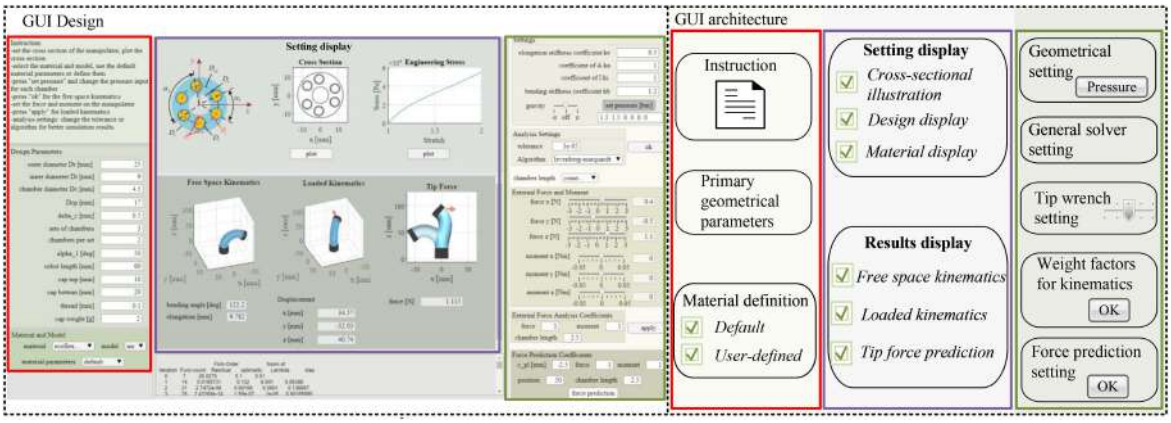

Fig. 4. Graphic user interface with its architecture for achieving analytical analysis of soft robots with densely reinforced chambers. Robot design parameters, simulation settings and results are highlighted in the red, green, and violet boxes, respectively. A detailed instruction of using the GUI can be found in Section S.IV of the Supplementary Material (see Figs. S7– S12) and the Supplementary Video. The GUI toolbox can be downloaded from the GitHub repository [58], upon request by completing the form at https://forms.gle/DJNQDFSh3SVtjVKv6.

Algorithm 2: Planar Force Generation.

Input: pressure P, the material model and parameters, robot dimensions, displacement h, weight coefficients W_n, W_m, W_L and W_h.

Output: position vector $p(s)$, rotation matrix $R(s)$, blocked force F_b, and new chamber lengths L_c^i from the constrained shape.

Initialisation: cross-sectional geometries $A_0, I_{x,0}, I_{y,0}, J_{z,0}$, initial guess $g(0)$, convergence tolerance ϵ;

$L_c^i \leftarrow$ save the chamber lengths in the free-space by solving **Algorithm 1:** *Free_space_kinematics()*;

$(L_c^i)_{P^i} \leftarrow$ select the length of pressurised chambers from the free-space kinematics ($P^i > 0$);

while $e \geq \epsilon$ **do**

  $n(L), m(L), H_p, L_c^i \leftarrow$ integrate (17) using $g(0)$ via the Fourth-order Runge-Kutta method, with $g(0) = [n(0), m(0), F_b]$;

  $(L_c^i)_{F_b} \leftarrow$ select the new length of pressurised chambers;

  $e \leftarrow$ evaluate errors from the boundary conditions (14), (15), (16) and (18);

  update $g(0)$ via the Levenberg–Marquardt method;

end while

return $(L_c^i)_{F_b}, p(s), R(s), F_b$;

Algorithm 1 needs to be solved first and returns the chamber lengths which are used as the constraints [see (14)]. Equation (17) is then integrated again by satisfying the new boundary conditions (14)–(16) and (18), which eventually returns the estimated force F_b. In Algorithms 1–2, the Levenberg–Marquardt method can be used to update the initial guess $g(0)$. Meanwhile, the Fourth-order Runge–Kutta method is adopted to integrate the ODEs.

III. Analysis and Evaluation Framework

Apart from the static analytical modeling framework presented in Section II, the analysis and evaluation framework is then elaborated in this section, including the design of a GUI toolbox for model-based analysis and a physical platform for experimental evaluation for soft robots.

A. Simulation Toolbox for Robot Design

To achieve a user-friendly robot evaluation when design parameters vary, a MATLAB-based software was developed. This software can be downloaded from the GitHub repository [58], upon request by completing the form at https://forms.gle/DJNQDFSh3SVtjVKv6. The software is based on the analytical modeling framework proposed in Section II, and its architecture and GUI outlined in Fig. 4. The architecture can be divided into three parts, including parameter definition (within the red rectangles), solving setting (within the green rectangles), and results display (within the purple rectangles). The following sections provide a brief instruction of the GUI.

1) Parameter Definition: The geometrical design parameters (e.g., the outer diameter from Table II) and actuation chamber numbers, can be defined by the user. The bottom block is used to choose types of silicone materials and the corresponding (non)linear material models. Apart from the Ecoflex 00-50, the default material database includes other commonly used silicone materials, Ecoflex 00-10, 00-20, 00-30, and Dragon Skin 10 (slow). Five material models are included: the linear material model, NH model, MR model, Yeoh model, and Odgen model. The model parameters are summarized in Table I (see Supplementary Material for more details). In addition, users can adjust parameters of five predefined material models based on their identification results. To accommodate for a broader range of compliant materials, such as customized elastomers, or 3D-printed materials like TPU or TPE, the GUI allows users to define their own stress–strain functions and corresponding parameters. Details of user-defined material models are reported in the Supplementary Document and the Supplementary Video.

2) Solving Setting: These settings include the geometrical compensation coefficients for A and I, and the stiffness coefficients k_e and k_b when considering the chamber stiffening effect. The direction of gravity can be set along the $-z$-, $+z$-axis, or as off using a slider. The solver setting chooses the optimization algorithms for the shooting method and sets the convergence tolerance. The tip force and moment can also be

TABLE II
GEOMETRICAL PARAMETERS AND DIMENSIONS OF DIFFERENT ROBOTS, AS SHOWN IN FIG. 1(a)

Symbols	Description	Robot							
		D25L40	D20L40	D15L40	D10L40	D25L60	D20L60	D15L60	D10L60
L_c	Length of the fibre-reinforced chamber [mm]	40.0	40.0	40.0	40.0	60.0	60.0	60.0	60.0
D_r	Diameter of the robot [mm]	25.0	20.0	15.0	10.0	25.0	20.0	15.0	10.0
D_i	Diameter of the central channel [mm]	9.0	7.2	5.4	3.0	9.0	7.2	5.4	3.0
D_{cp}	Diameter of the positioned chamber [mm]	17.0	13.6	10.2	6.5	17.0	13.6	10.2	6.5
D_c	Diameter of the chamber [mm]	4.5	3.6	2.5	1.5	4.5	3.6	2.5	1.5
δ_c	Wall thickness of the chamber [mm]	0.5	0.5	0.5	0.5	0.5	0.5	0.5	0.5
δ_r	Minimum depth of the embedded thread [mm]	1.25	0.9	0.65	0.5	1.25	0.9	0.65	0.5
α_1	Angle between two adjacent chambers [°]	50.0	50.0	56.0	60.0	50.0	50.0	56.0	60.0
α_2	Angle between every other chamber [°]	120.0	120.0	120.0	120.0	120.0	120.0	120.0	120.0

* $D * L\#$ is used to label different robots, where $*$ and $\#$ denote the initial outermost diameter of robots and the initial length of the chamber. Please note that the CAD files and printing details of the moulds for all robots are openly accessible in the Git Repository [58].

set to investigate how the robot deflects under external loads. Finally, the bottom shows the weight factor setting for better scaling of the shooting problem [see (18)]. Please note the influence of chamber constraints can be turned-ON or OFF.

3) Results Display: The design and simulation results are displayed. After defining the design parameters, the settings can be displayed, e.g., the cross-sectional geometry and the stress-stretch curve of material, to check parameter settings. The results of the free-space kinematics, loaded kinematics (considering external tip loads) and tip blocked force are presented in the bottom-middle of the software interface.

The proposed static modeling framework is fully encapsulated into the GUI. Main features of the GUI are as follows.

1) *Versatility:* The user can select and define design parameters (presented in Table II), type of material models and its parameters, influences of actuation chambers, and solver settings.
2) *Visualization:* The settings and simulation results are displayed. This user-friendly interface allows users to explore a simulation-based robot design and achieve comparisons and evaluations, e.g., kinematics and tip force generation capability, based on design parameters.

B. Evaluation Platform for Soft Robots

To further achieve an experimental evaluation of soft robots, a physical platform is presented [65]. The platform and its architecture are shown in Fig. 5. The hardware comprises pressure regulators (Camozzi K8P, 0–3 bar) for setting the actuation pressure, an NI USB-6341 (National Instruments DAQ) for high-speed data acquisition, an microcontroller (Arduino DUE) for real-time control, an electromagnetic (EM) tracking system (NDI Aurora) for recording the position and orientation of robots, a force/torque (F/T) sensor (IIT-FT17) for force capability identification.

The architecture of the platform [see Fig. 5(b)] is as follows.

1) The first floor includes the 220 V ac power units and an ac–dc converter providing 5 V, 12 V, and 24 V dc power. In addition, protection circuits and overcurrent fuse are included.
2) The second floor is for low-voltage ($\leq$ 24 V) electronics. Pressure regulators control and monitor the chamber pressure; the microcontroller communicates with two DAC converters (Adafruit MCP4728) via I2C to set pressure control signals (0–10 V).

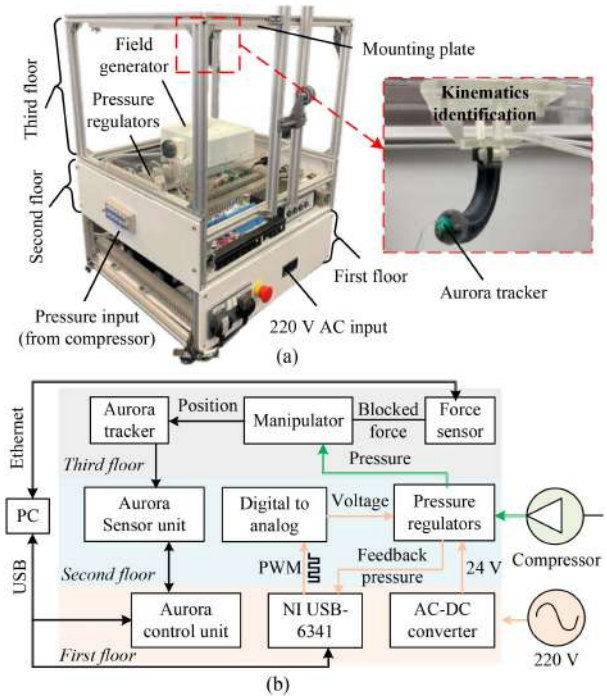

Fig. 5. Experimental evaluation platform. (a) Structure. (b) Electrical architecture of the platform.

3) The third floor contains the field generator (NDI), the F/T sensor and structures for positioning robots.

Please note that the EM trackers are compact and offer high accuracy (e.g., position error of 0.7 mm, angular error ≤ 0.5 degree), well-suited for robot characterization. In addition, our platform supports alternative tracking options, such as camera-based systems, if required. For example, a dual-camera setup was in [66], where two cameras were used to estimate interaction forces between the robot and its environment.

To summarize, the proposed framework includes the analytical models from Section II, the GUI toolbox for model-based analysis and the physical platform for experimental evaluation of soft robots.

IV. EXPERIMENT AND VALIDATION OF THE PROPOSED FRAMEWORK

The validation of the proposed modeling, design, and evaluation framework is conducted in this section. Following the robot

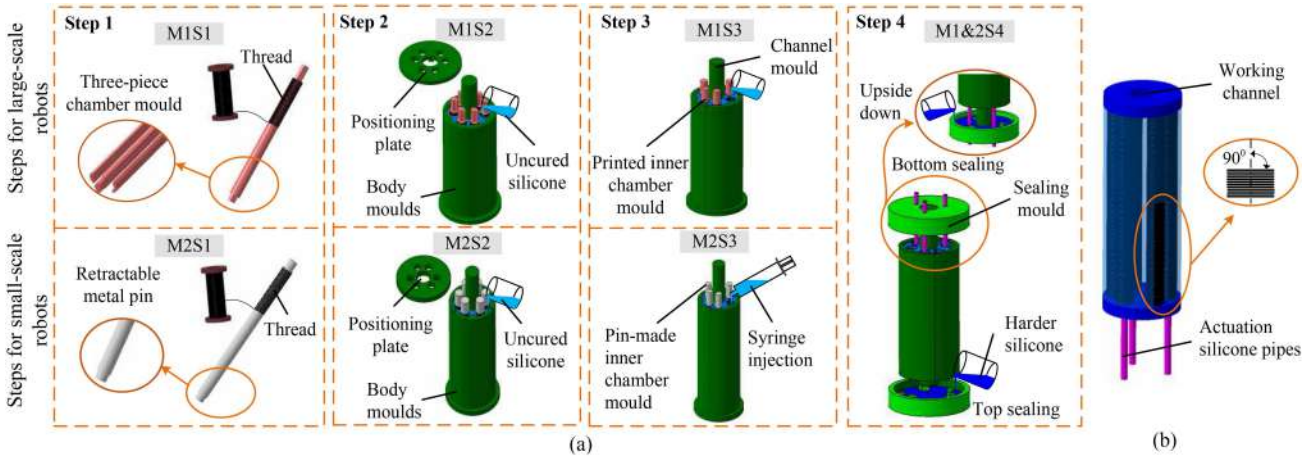

Fig. 6. (a) Two Fabrication paradigms M1 and M2, for fabricating large-scale robots (diameter $\geq$ 15 mm) and small-scale robots (diameter $<$ 15 mm), respectively. Step 1: densely weaving the thread to printed three-piece chamber moulds (M1S1) or retractable pins (M2S1); step 2: pouring the silicone to assembled moulds to make the main body of robots (M1S2 and M2S2); step 3: fabricating the inner layer of the chambers via pouring silicone (M1S3) or syringe injection (M2S3); step 4: sealing the top and bottom of robots (M1&2S4). (b) Structure details of the robots with densely reinforced chambers.

morphology in Section II-A, a general fabrication process is presented. Eight types of robots are then fabricated, using four diameters (10 mm, 15 mm, 20 mm, 25 mm) and two lengths (40 mm and 60 mm). All the robots are used to evaluate and validate 1) the robot kinematics and 2) the tip force generation. All the experiments were conducted using the physical evaluation platform presented in Section III-B.

A. Robot Fabrication

Two fabrication paradigms, Method 1 (M1) and Method 2 (M2), are generalized in Fig. 6, to manufacture soft robots with different dimensions. Specifically, M1 is more suitable for fabricating large-scale robots, i.e., the diameter is equal or larger than 15 mm. While M2 is more applicable for robots with a diameter smaller than 15 mm. M1 and M2 comprise a four-step fabrication procedure (S1–S4 in Fig. 6).

In M1S1, three-piece chamber moulds (coloured in pink) are 3D-printed and assembled before weaving the reinforced thread. This three-piece design facilitates the removal of chamber moulds in M1S2. Nevertheless, the reduced chamber dimensions of small-scale robots make 3-D printing unsuitable for producing pieced moulds. In such case, retractable metal pin (coloured in grey) is proposed and shown in M2. The pin can be removed easily for its small diameter (less than 3 mm) and smooth surface. In step 2, the silicone is poured into the assembled moulds with 3-D printed main structures (colored in green). The chamber moulds are removed once the silicone cures. In step 3, the silicone is poured to the chambers and smaller chamber moulds are inserted to form the inner silicone layer of the reinforced chambers. It is worth noting that the viscosity of silicone makes it hard to fill chambers of small-scale robots, syringe injection then can be used to avoid this issue, as shown in Fig. 6 (M2S3). In step 4, the actuation pipes are added and robots are sealed by a harder silicone (colored in dark blue), which is the same for M1 and M2. Fig. 6(b) illustrates the structure details of the robots.

Eight types of robots were fabricated using Ecoflex 00-50 (Supersoft, SmoothOn), as shown in Fig. 7(a). Ecoflex 00-50 was

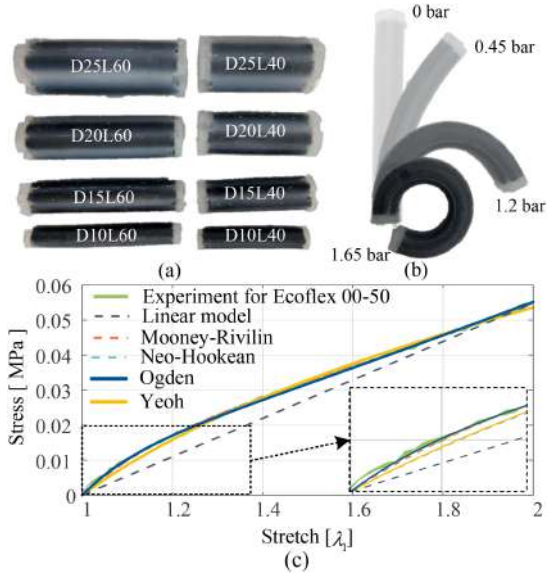

Fig. 7. Eight soft robots made of Ecoflex 00-50. (a) Robots with lengths of 40 mm and 60 mm, diameters of 10 mm, 15 mm, 20 mm, and 25 mm. (b) Bending motion of the D10L60 robot. (c) Tensile test for Ecoflex 00-50.

selected for physical prototyping because it offers a moderate shore hardness (see Table II), balancing force output and range of motion. This allows us to benchmark modeling accuracy across varying robot dimensions at a consistent pressure level. In contrast, softer materials, such as Ecoflex 10 to 30 produce small forces, while stiffer materials like Dragon Skin 10 restrict motions of robots. Their detailed dimensions are summarized in Table II. The robots with diameters of 10 mm are fabricated using M2, and the robots with diameters of 15 mm, 20 mm, and 25 mm are fabricated using M1. The robots are labeled as $D * L\#$, where $*$ refers to the diameter D_r and $\#$ is the chamber length L_c. The printed parts of the moulds for all robots are accessible in the Github repository. For small-scale robots, the bending angle can be larger than 300°, as shown in Fig. 7(b).

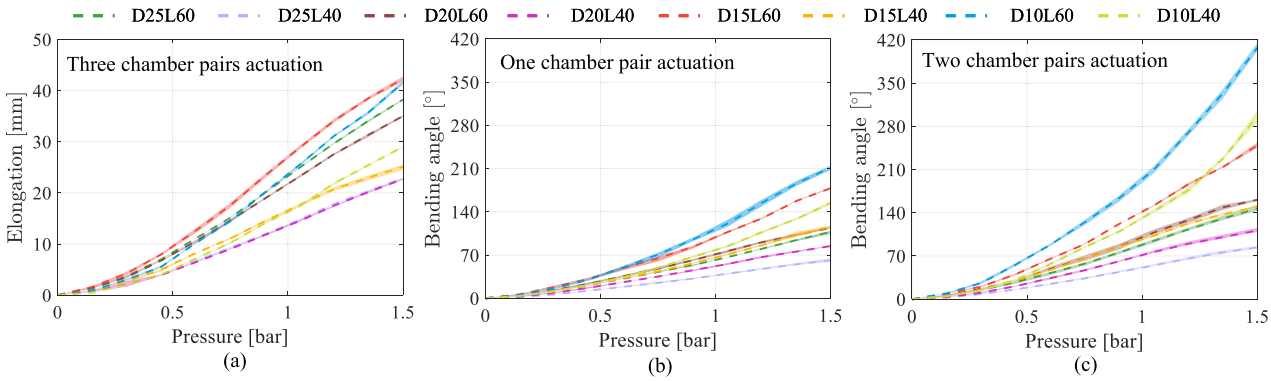

Fig. 8. Results of the bending and elongation tests with the actuation pressure in the range [0–1.5] bar. (a) Elongation from actuation of three chamber pairs, bending from actuation of (b) one chamber pair and (c) two chamber pairs. The shaded error regions represent the variability across the three trials conducted for each test.

B. Evaluation and Validation of Robot Kinematics

1) Validation Protocol: The kinematics evaluation and validation were conducted through both experiments and simulations. During the experiments, the NDI EM tracking system can monitor the tip position and orientation of the robot by the attached tracker (see Fig. 5). In simulation, five material models (see Section II-E) were all implemented and compared, where the pressure collected from the experiments were the input to the simulation models. Eight types of robots were used to validate their bending and elongation capabilities and the workspace.

a) *Evaluation and validation of the elongation and bending of soft robots:* In the elongation test, all the chambers were actuated; in the bending test, one chamber pair and two chamber pairs were actuated. The actuation pressure was incremented from 0 to 1.5 bar, in steps of 0.15 bar. Each test repeated three trials.

b) *Evaluation and validation of the workspace of soft robots:* The pressure in each chamber of soft robots varied alternately and was capped at 1.2 bar during 0–260 s. The experimental tip positions were compared with the simulation results each second, obtaining 260 examined points for each trial. The differences of the robots' tip position between the simulation and experiment in the Cartesian space are defined as the modeling errors.

2) Results for Elongation and Bending: Fig. 8(a)–(c) presents the experimental evaluation results for all the robots undergoing bending and elongation motions. The average elongation for the L60 robots ranges from 35.03 to 42.31 mm, with elongation ratios (with respect to the chamber lengths) of 0.58–0.71. By contrast, the elongation for the L40 robots is between 22.70 mm and 25.11 mm, with similar elongation ratios of 0.57–0.63. For bending tests, Fig. 8(c) demonstrates that the robots with two chamber pairs actuated consistently show a larger bending angle compared with that from actuating one chamber pair. For example, the maximum bending angles under actuation of two chamber pairs for the D10L60, D15L60, D20L60, D25L60 robots are 413.33°, 249.01°, 161.03°, and 147.05°. While for actuation of one chamber pair, corresponding values are 211.67°, 178.41°, 118.57°, and 107.67°. Moreover, the bending and elongation responses are nonlinear and generally flatted under a high pressure (especially for the D25 and D20 robots).

The comparisons between experiment and simulation data from five material models are reported in Fig. 9(a)–(c), with the absolute errors reported in box plots. Fig. 9(a) illustrates the elongation error, where the linear material model exhibits an inferior accuracy, with the median values between 2.0 and 8.0 mm. In contrast, hyperelastic models show a better performance with maximum and median errors below 3.0 and 2.5 mm. Moreover, Fig. 9(b) reports the bending errors when actuating one chamber pair. Overall, the errors from the linear material model are the largest, with median values above 20.0° and a maximum error of 48.7° from the D10L60 robot. By comparison, the median errors for hyperelastic models are below 20.0°. Furthermore, their median and maximum errors are below 10.0° and 20.0° in most cases. Similar median bending errors are observed from Fig. 9(c), where two chamber pairs are actuated, e.g., less than 10.0° from the hyperelastic models, while with larger maximum errors (especially for the D15 and D10 robots).

The raw data of the D25L60 and D10L60 robots are in Fig. 9(d) and (e), respectively. The linear material model predicts an approximately linear response. The hyperelastic models are capable of predicting the nonlinear responses. Under low pressurization levels, the Odgen and Mooney–Rivlin model have similar results. By contrast, the Yeoh model and Neo-Hookean model have similar but larger predicted values. The Ogden and Mooney–Rivlin models tend to diverge under high pressurization levels, where the Ogden model has larger predicted bending angles, especially for the D10L60 robot.

Fig. 10 reports the results with and without considering chamber stiffening (see Section II-C) of the D25L60 robot. The chamber stiffening effect is generally less obvious when the pressure is low, e.g., less than 0.5 bar. Furthermore, the results then illustrate that considering the stiffening effect can improve the accuracy when the pressure increases. Specifically, the simulation diverges from the experiment under a high pressure level, e.g., larger than 1 bar, when the chamber stiffening is not considered, especially when two [see Fig. 10(c)] and three [see Fig. 10(a)] chamber pairs are actuated.

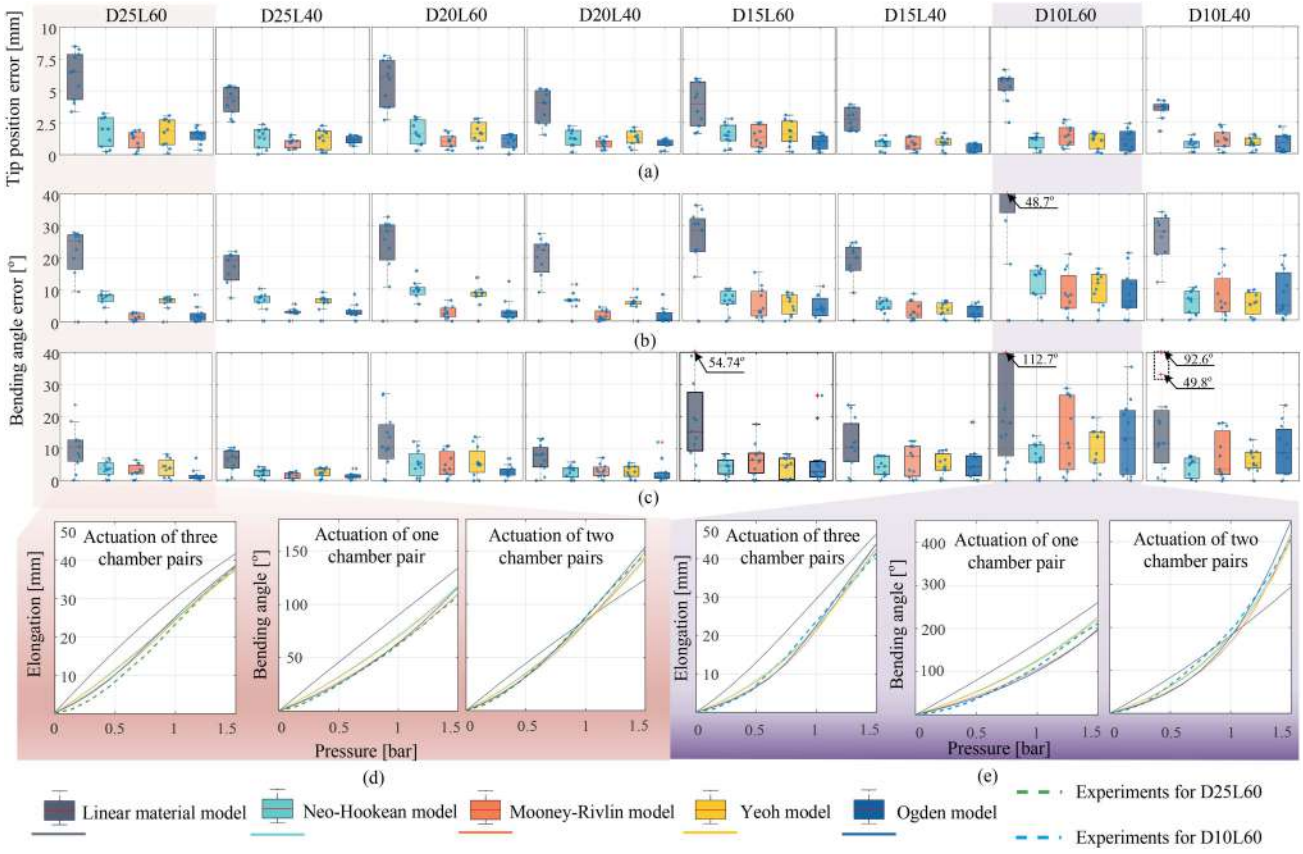

Fig. 9. Results of the bending and elongation comparisons across five models and experiments, with absolute errors boxplotted. The results from one, two and three chamber pair(s) actuation are shown in (a), (b), and (c). Detailed comparisons of the experiment and simulation for the D25L60 and D10L60 robots are plotted in (d) and (e), with the whole comparisons shown in Figs. S2– S3 from the Supplementary Material.

3) Results for Workspace: Fig. 11(a) illustrates the actuation pressure sequences for three pairs of chambers. The tips position errors for all the robots are summarized in Fig. 11(b)–(e). Four hyperelastic models exhibit similar performances, and the median tip position errors of all the L60 and L40 robots are smaller than 10 mm and 5 mm, respectively. By contrast, the linear material model has larger median errors. Moreover, the linear material model also has larger maximum errors, i.e., larger than 25 mm for the L60 robots and 15 mm for the L40 robots. Focusing on the D25 and D20 robots, the Ogden model has the smallest median error. However, this becomes less obvious for the D15 and D10 robots. In general, the modeling errors increase when robots have smaller diameters and longer lengths.

C. Evaluation and Validation of the Tip Force Generation

1) Validation Protocol: The tip force generation model from Section II-D is validated using eight types of robots. The pressure in one chamber pair was set in the range of 0–1.5 bar, with increments of 0.3 bar. Each measurement had three repetitive trials. The tip of the robot was constrained by the F/T sensor to measure the blocked force. A disk can be attached to the force sensor. In all experiments, the disk was positioned directly beneath the robot. As such, when no actuation pressure is applied, the distance between the disk and the robot's central axis equals the robot's radius [see Fig. 12(e)]. Since the evaluation of the kinematics demonstrates that the linear material model is significantly inferior to the four hyperelastic models, this section focuses on the evaluation of the hyperelastic models. The results are in Figs. 12, 13, and Table III.

2) Results for the Tip Force Generation: Fig. 12(a) and (b) reports the snapshots of the force measurement for the D25 and D10 robots. Robots with longer lengths and smaller diameters show a larger deformation under the same pressure level. Fig. 12(d) demonstrates the simulated and experimental shapes of the D25 and D10 robots when the actuation pressure is 1.5 bar, which demonstrates a high fidelity of the tip force generation model. Moreover, the model is still applicable when the robots have large deformations, e.g., the bending angle of the D10L60 robot in the free space is over 220°.

Fig. 13 reports experiment results of the tip force generation for all robots and the simulated results from the hyperelastic models. The results highlight that the force and pressure have a strong linear relationship, which is independent from the diameter and length of robots. Furthermore, comparing Fig. 13(a)–(d), it is observed that the generated force is smaller when the diameter of the robot decreases. For example, the maximum generated forces for the D25L60, D20L60, D15L60, and D10L60 robots are 1.18 N, 0.71 N, 0.34 N, and 0.10 N, respectively. Focusing on robots with the same diameter, the length of the robot has a less influence on the force generation compared to the diameter. Specifically, the maximum forces are 1.27 N, 0.82 N, 0.39 N,

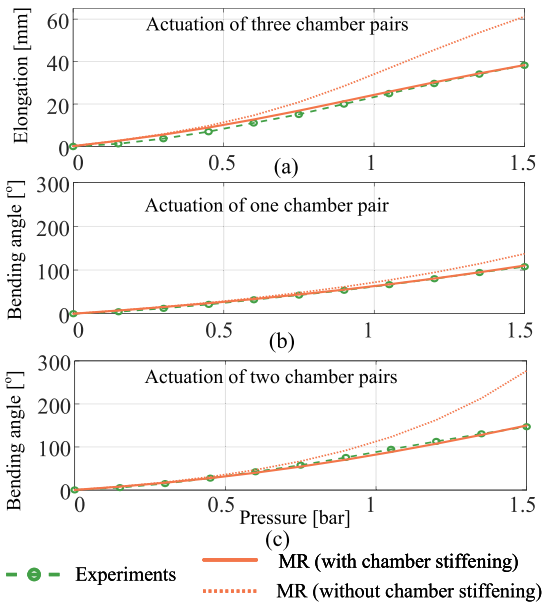

Fig. 10. Comparison between with and without chamber stiffening (see Section II-C). The results are exemplified using the D25L60 robot and Mooney–Rivlin model. The results of actuating one, two, and three chamber pairs are shown in panels (a), (b), and (c), respectively.

TABLE III
RESULTS FOR THE TIP FORCE GENERATION: ERROR SUMMARY (RMSE AND MAPE) OF THE TIP FORCE PREDICTION USING HYPERELASTIC MODELS

Robot	RMSE&MAPE for different models [N]				Force [N] @1.5 bar
	NH	MR	Yeoh	Ogden	
D25L60	0.039 (4.17%)	0.025 (3.05%)	0.029 (3.91%)	0.031 (4.58%)	1.18
D25L40	0.032 (6.74%)	0.034 (6.23%)	0.033 (6.79%)	0.035 (6.26%)	1.27
D20L60	0.037 (5.06%)	0.026 (6.50%)	0.035 (4.69%)	0.037 (8.62%)	0.71
D20L40	0.022 (6.26%)	0.013 (3.59%)	0.018 (5.43%)	0.015 (3.71%)	0.82
D15L60	0.0098 (4.48%)	0.0024 (10.84%)	0.012 (5.02%)	0.025 (13.46%)	0.34
D15L40	0.033 (7.60%)	0.016 (4.32%)	0.028 (6.24%)	0.022 (6.98%)	0.39
D10L60	0.015 (13.97%)	0.011 (16.02%)	0.017 (15.89%)	0.013 (18.96%)	0.10
D10L40	0.010 (13.77%)	0.017 (23.52%)	0.011 (15.65%)	0.018 (23.79%)	0.12

* RMSE is the Root Mean Square Error (N) and MAPE is the Mean Absolute Percentage Error (%).

and 0.12 N for the D25L40, D20L40, D15L40, and D10L40 robots, respectively.

Fig. 13 shows that four hyperelastic models can predict the blocked force, with different accuracy. In general, the Mooney–Rivlin and Ogden models show a similar accuracy, while the Neo-Hooken and Yeoh models behave alike. Table III summarizes the RMSE and MAPE results. Considering the tip force generation, the accuracy differences between four hyperelastic models are less obvious than those from the results of kinematics, especially for robots with larger diameters. For example, the differences of the MAPE are less than 1% for the D25 robots. For large-scale robots, i.e., the D15-D25 robots, better accuracy is observed. In general, the MAPE values are between 3% and 10%. In contrast, for the D10 robots, the error is larger and the MAPE is between 13% and 24%. The RMSE values are between 0.01 and 0.04 N for all robots.

Fig. 14(a) and (b) compares the tip force generation results with and without considering constraints of the pressurized chamber length, exemplified using the D25L60 robot and the MR model. Fig. 14(a) indicates a predicted force of 1.22 N, whereas Fig. 14(b) reveals a predicted force of 0.78 N, both under a consistent 1.5 bar actuation pressure. When compared with the average experiment value of 1.18 N, the corresponding errors are 3.39% (considering chamber constraints) and 33.90% (without considering chamber constraints), respectively.

V. CASE STUDY OF THE FRAMEWORK: DESIGN OF A SOFT ROBOTIC LAPAROSCOPE

The proposed and validated framework, including the analytical models and the evaluation platform, can be used for application-oriented robot design. As illustrated in Fig. 15, once the design specification and dimension constraints for a specific application are identified, the user can experiment with the GUI to preliminarily determine, e.g., main design parameters and material selection. This information can be used to expedite the robot design and reduce the prototyping time of robots. This section reports a case study of using the framework to design and evaluate a soft robotic laparoscope.

A. Medical Requirement of Laparoscopes

Laparoscopy is an MIS in which a surgeon uses a laparoscope (a small, camera-equipped instrument) inserted through tiny incisions to view and operate inside the abdomen or pelvis. During the procedure, trocars, typically less than 12 mm in diameter, are used to create access ports through these incisions, allowing the insertion of the laparoscope and other surgical instruments. Within this context, a soft laparoscope needs to satisfy the following.

1) Diameter smaller than 12 mm to fit standard trocars.
2) A free lumen of about 4 and 5 mm for feeding the laparoscopic camera mounted at the tip [25].
3) Omni-directional tip bending angle greater than 100 degrees over a tip length of 30–50 mm [67].
4) Adequate yet gentle force (e.g., 0.3–1 N) to support the tip-mounted camera without risking tissue damage [68].

In addition, our experimental platform can supply pressure up to 3 bar. Building on the above constraints, following sections demonstrate how the developed framework streamlines robot prototyping and enable rapid performance evaluation.

B. Determining Key Robot Parameters Using the Framework

To fit a 12 mm standard trocar port, the diameter of the robot D_r is set as 11.4 mm, with a margin of 0.6 mm. The diameter of

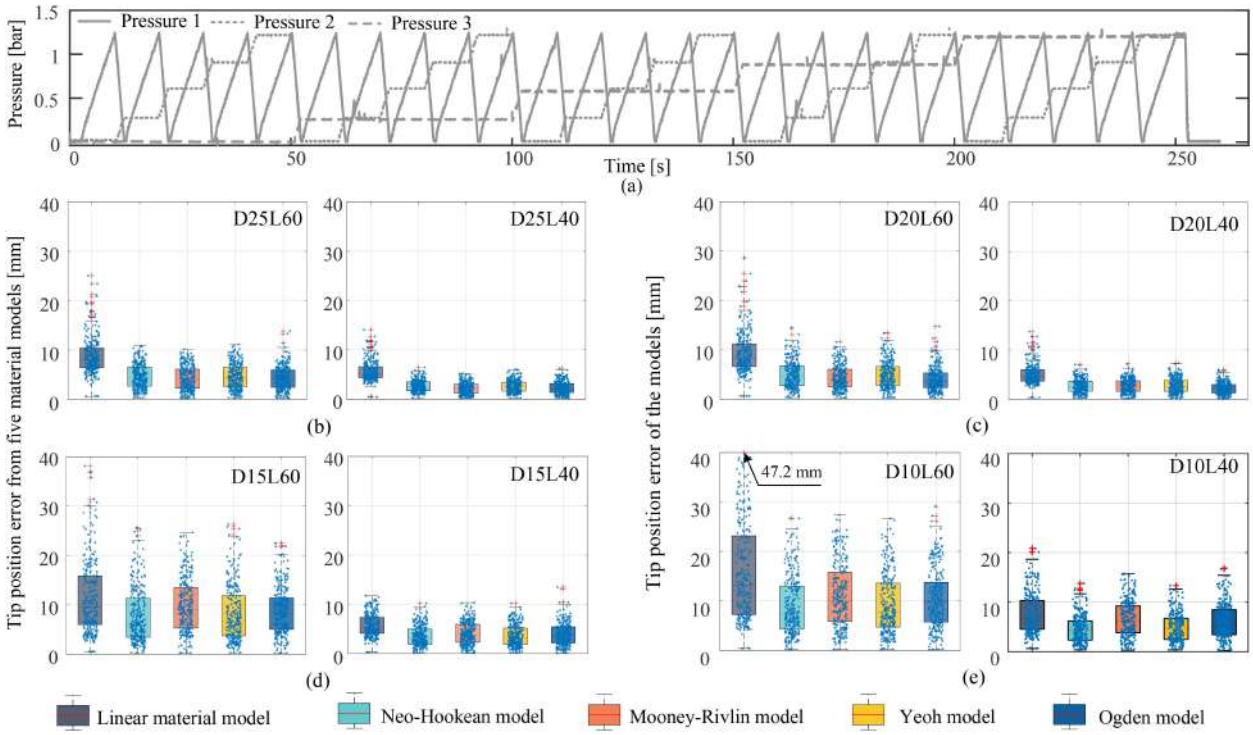

Fig. 11. Results for workspace validation of the methodology using five models, with the box plots of absolute Cartesian tip position errors. (a) Actuation pressure sequences for measuring the workspace. The summarized results for the D25, D20, D15, and D10 robots are shown in (b), (c), (d), and (e), respectively. The tip position errors at each point across the entire workspace for all robots are presented in Figs. S4– S6 of the Supplementary Material.

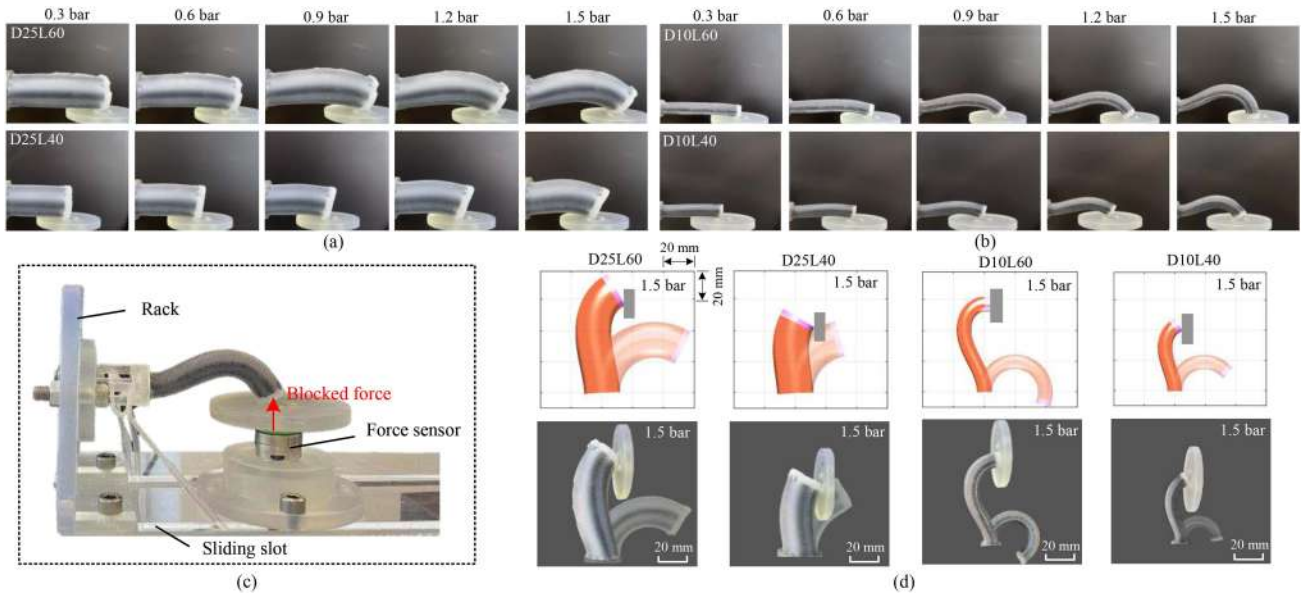

Fig. 12. Tip force measurement snapshots for the (a) D25 robots. (b) D10 robots. (c) Setup for measuring the tip force generation. (d) The comparisons between the simulations (using the Mooney–Rivlin model) and the experiments for the D25L60, D25L40, D10L60, and D10L40 robots when the pressure reaches a maximum value of 1.5 bar. The transparent figures are the poses when the robots are actuated in a free space, and the dark figures are the poses in a constrained space.

the central lumen D_i is set as 4.7 mm, and δ_c is set as a minimal value of 0.4 mm. Building on these dimensions, the cross section display in the GUI (see Fig. 4) then illustrates the maximum inner diameter of the actuation chamber D_c is 1.5 mm, and total numbers of actuation chambers can be 3, 6, and 9 paired in three sets. The robot length is set as 45 mm.

Using the dimensional parameters above, Table IV reports the simulated tip bending angles and tip forces of soft robots made of various silicone materials. In all simulations, one chamber set was actuated. Feasible designs (angle $\geq 100^\circ$) and infeasible designs (angle $\leq 100^\circ$) are coloured in blue and red, respectively. Ecoflex 10, 20, and 30 all satisfy the bending requirement within

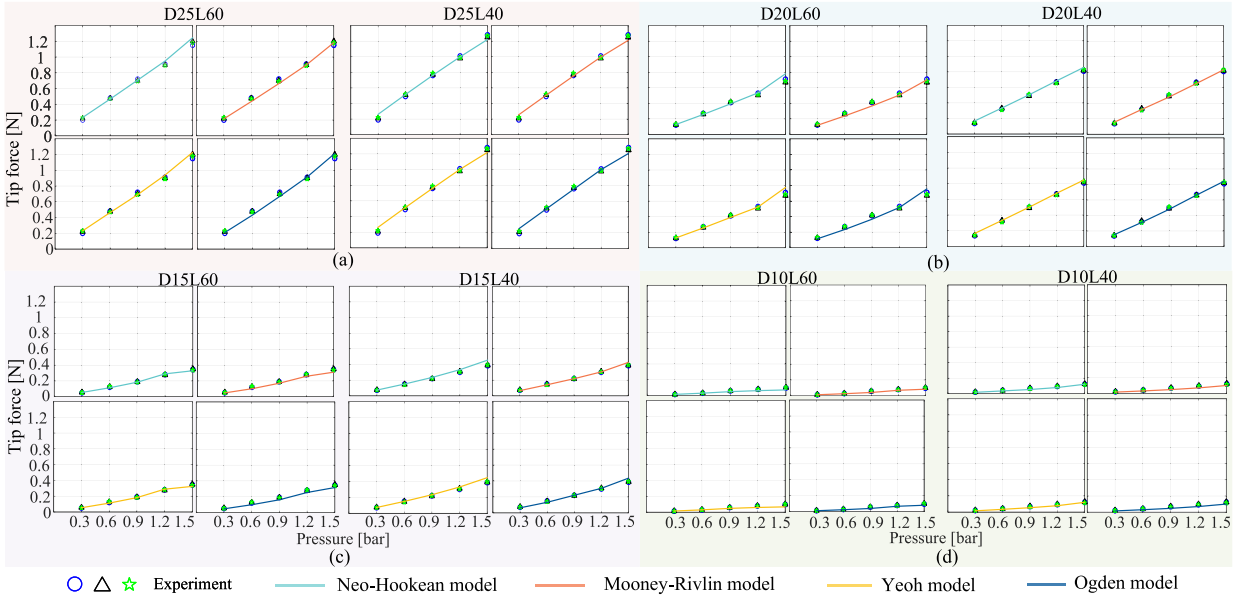

Fig. 13. Results of the tip force model: The comparisons between experimental force identification and simulated results from four hyperelastic models for the (a) D25, (b) D20, (c) D15, and (d) D10 robots with two lengths.

TABLE IV
PERFORMANCE COMPARISON OF ROBOTS WITH DIFFERENT SILICONE MATERIALS USING THE GUI

Total chambers	Results	Ecoflex 10	Ecoflex 20	Ecoflex 30	Ecoflex 50	Dragon Skin 10
9 chambers	Angle [deg]	112.7° @ 0.4 bar	133.2° @ 0.6 bar	113.9° @ 0.8 bar	108.9° @ 1.2 bar	105.6° @ 3.0 bar
	Force [N]	0.038 N @ 0.4 bar	0.050 N @ 0.6 bar	0.055 N @ 0.8 bar	0.161 N @ 1.2 bar	0.380 N @ 3.0 bar
6 chambers	Angle [deg]	111.6° @ 0.6 bar	111.7° @ 0.8 bar	113.4° @ 1.2 bar	108.5° @ 1.8 bar	62.5° @ 3.0 bar
	Force [N]	0.034 N @ 0.6 bar	0.078 N @ 0.8 bar	0.111 N @ 1.2 bar	0.180 N @ 1.8 bar	0.266 N @ 3.0 bar
3 chambers	Angle [deg]	107.0° @ 1.2 bar	107.7° @ 1.6 bar	109.2° @ 2.4 bar	82.2° @ 3.0 bar	27.7° @ 3.0 bar
	Force [N]	0.032 N @ 1.2 bar	0.040 N @ 1.6 bar	0.125 N @ 2.4 bar	0.184 N @ 3.0 bar	0.106 N @ 3.0 bar

* The Mooney–Rivlin model is used in all simulations. Blue regions indicate feasible designs with sufficient bending motions, while red regions represent infeasible ones. Green regions highlight the feasible design in each row that achieves the highest output force.

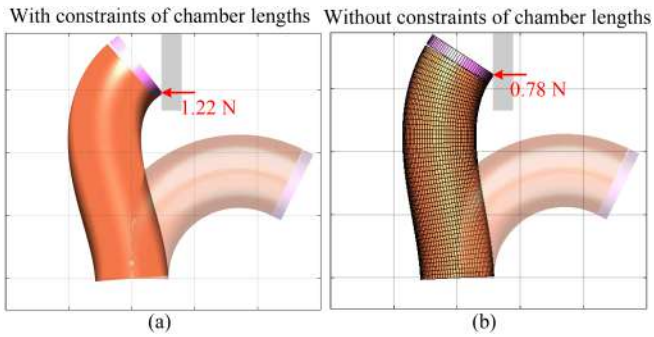

Fig. 14. Simulation comparisons of the force generation (a) with and (b) without chamber constraints defined in (14) and illustrated in Fig. 3. The results are exemplified using the D25L60 robot and the Mooney–Rivlin model. The chamber pressure is set as 1.5 bar. The transparent figures denote the pose of the robot in a free space.

an actuation pressure of 3 bar, though the resulting tip forces range only from 0.03 to 0.13 N. When using Ecoflex 50, the optimal design is a robot with six chambers arranged in three sets, achieving a tip force close to 0.2 N at 1.8 bar. In comparison, the robot made from Dragon Skin 10 with 9 chambers in three sets demonstrates the best overall performance, producing a maximum tip force of 0.38 N and a bending angle exceeding 105.6°, making it the most suitable for application requirements detailed in Section V-A.

C. Fabrication and Evaluation of the Soft Laparoscope

Based on parameters determined in Section V-B, the fabrication paradigm M2 (see Fig. 6) is adopted to fabricate the 11.4 mm robot. All moulds are 3D-printed, and the CAD files are available in the Git repository. Diameters of two types of metal pins are 2.3 mm 1.5 mm. Dragon Skin 30 is used to seal both ends of the robot. The fabricated robot and its cross section are reported in Fig. 16(a).

The platform in Fig. 5 was used to evaluate the robot. An EM sensor was mounted at the robot's tip to measure bending angles under actuation of both one and two chamber pairs, with pressures ranging from 0 to 3 bar. To characterize the tip force, the same setup described in Fig. 12 was employed. Finally, the soft laparoscope, integrated with a 4 mm tip-mounted camera (OV9734), was demonstrated in a 1:1 human phantom model with a conventional surgical grasper.

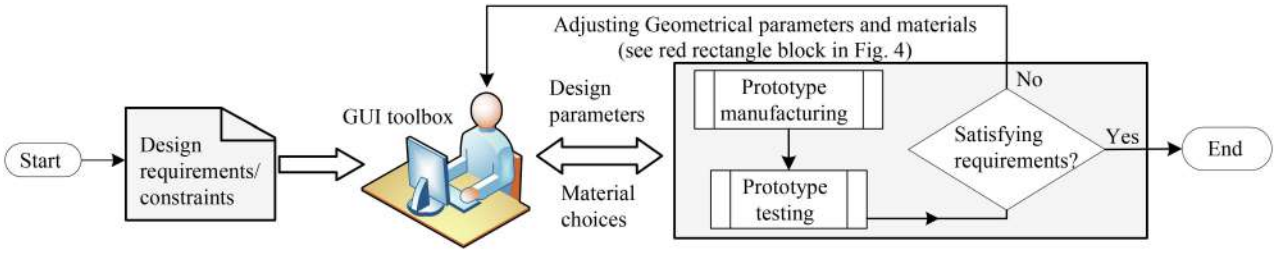

Fig. 15. Work flow of using the proposed framework to reduce robot prototyping time when design requirements are identified. The GUI can primarily determine main design parameters of the robot, as demonstrated in Table IV.

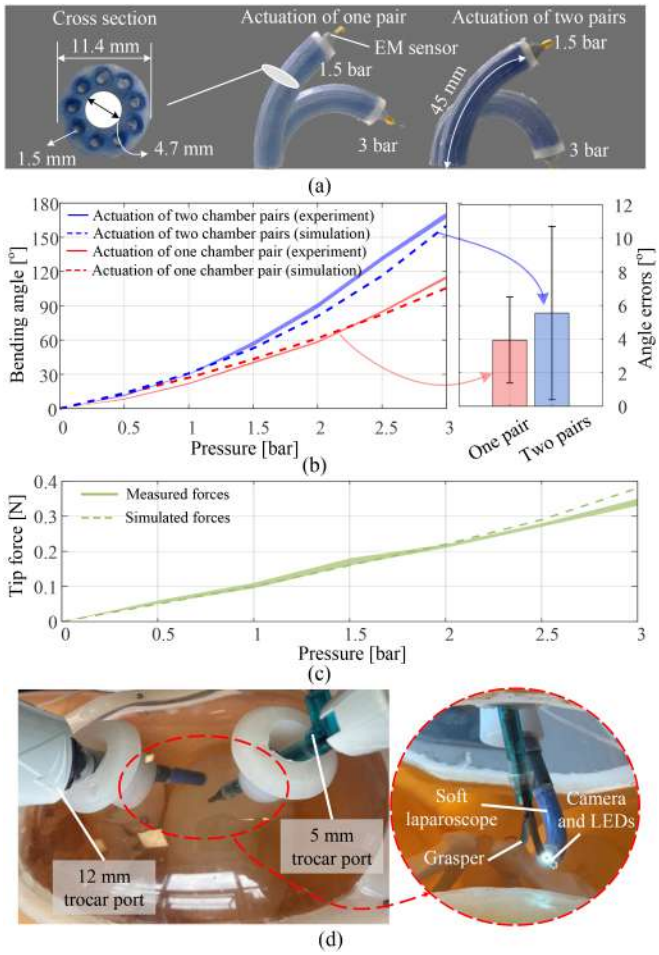

Fig. 16. Results for the case study. (a) Dimension details of the robot. (b) Simulated and experimental bending angles of the soft manipulator. Summarized average modeling errors are barplotted on the left. (c) Simulated and measured tip forces. (d) Demonstration of the soft laparoscope in a phantom.

Fig. 16(b) presents the experimental and simulated bending angles from two tests: actuation of one chamber pair and actuation of two chamber pairs. Each test repeated three trials. The maximum bending angles achieved are 115.0° and 169.3° for the one- and two-pair actuations, respectively. The corresponding average modeling errors are 3.9° and 5.6°. In addition, Fig. 16(c) shows the tip forces, with maximum measured and simulated values of 0.34 N and 0.38 N, respectively. The model's MAPE in force prediction is 5.32%. Fig. 16(d) further illustrates the deployment of the developed laparoscope in the phantom setting.

Results in Fig. 16 confirm that the bending angles and force capability satisfy design requirements in Section V-A, following the work flow in Fig. 15. These results highlight that guided by the high-fidelity models and user-friendly GUI, design parameters of the soft laparoscope can be determined prior to the robot prototyping.

VI. Discussions

As highlighted in Table V, our work presents an integrated framework for the fabrication, modeling, and evaluation of soft robots with reinforced chambers. Furthermore, we provide accessible hardware and software resources to help democratize research in this field. We also showcase the application of the framework to determine key design parameters of a soft robotic laparoscope. In contrast, existing work has typically focused on individual aspects, such as robot fabrication [11], modeling [43], control [51], and inverse shape-matching [52].

1) Discussions of the Robot Design and Fabrication: Fully fibre-reinforced chambers increase the robustness and repeatability of soft robots [57]. In particular, the pressurized circular chambers generate negligible radial expansion and do not squeeze other channels. This is different from, e.g., [18], [19] and could mitigate kinematics inconsistency. Another challenge is to miniaturize dimensions of the soft robots, for instance, a suitable size for fitting the trocar ports (e.g., 10–12 mm) in MIS, while preserving working channels [16]. The miniaturization of these robots is still desired to meet the clinical requirements [70]. For example, the smallest STIFF-FLOP manipulator has a diameter of 14.5 mm, with circular [25] or semicircular chambers [22]. Our generalized fabrication process in the framework (see Fig. 6) addresses this challenge, e.g., the diameter of such robot for the first time can be miniaturized to 10 mm while preserving a 3 mm central channel, by introducing the pin moulds and silicone injecting. This improves the dimension scalability when fabricating soft robots on different scales. In addition, the fabrication framework further guides design of subcentimetre soft manipulators of 7.8 mm diameter [71]. In addition, our framework provides a robot design toolbox by offering a simulation software with a GUI. This provides conveniences to preliminarily determine design parameters and tailor robots to different applications, as demonstrated in Section V. In addition, a soft instrument with a 11.5 mm diameter is developed in [28] for cancer imagining and in [8] for handheld laparoscopy, thanks to findings from the proposed framework.

For the design and evaluation of soft robots, we developed a user-friendly GUI built on the analytical models to achieve a

TABLE V
COMPARISON BETWEEN OUR FRAMEWORK AND EXISTING TOOLS FOR SOFT CONTINUUM ROBOTS

References	Actuation	Fabrication Guideline	Characterization and control hardware	Modeling Methodology	GUI for Robot Design	Open Accessibility	Main Research Interest
[11]	Pneumatics	Provided	Not provided	Analytical model	Not provided	Hardware	Robot fabrication
[43]	Hybrid	Not provided	Not provided	Analytical model	Not provided	Software	Robot modeling
[51]	Pneumatics	Not provided	Not provided	FEM	Not provided	Software	Robot modeling and control
[52]	Pneumatics	Not provided	Not provided	FEM	Provided	Software	Inverse design (shape-matching)
[69]	Pneumatics	Provided	Not provided	FEM	Not provided	Hardware and software	Online tutorials
Our work	Pneumatics	Provided	Provided	Analytical model	Provided	Hardware and software [58]	Robot modeling and evaluation

model-based evaluation and a physical platform for experimental evaluation. The reproducibility and consistency of soft robot fabrication remain a challenge in the field. This work enhances reproducibility by using dense fibre-reinforcement with threads placed at 90° related to the axial direction of soft robots, ensuring no gaps during manual thread preparation. CAD files for all moulds are shared in the Git repository to further improve reproducibility, though variations may still arise from mould manufacturing techniques, curing conditions of silicone, and reinforcement materials.

2) Discussions for Forward Kinematics: In theory, when the robot's cross-sectional dimensions are scaled by a factor of α and the actuation pressure is similar, the corresponding elongation ratio is almost not impacted while the bending curvature is approximately scaled by a factor of $1/\alpha$. As such, when soft robots have a similar elongation capability (assessed by the elongation ratio), the robots with smaller diameters achieve a better bending capability [see Fig. 8(b) and (c)]. This makes slender robots have enlarged workspace. Fig. 8 also demonstrates the bending and elongation motions are both nonlinear with respect to the actuation pressure. These nonlinearity results from the hyperelasticity of the silicone material and the influences of the chamber stiffening [59]. As such, the hyperelastic models outperform the linear material model. Moreover, the NH model and Yeoh model have larger predicted values compared to the results from the MR model and Ogden model. This is because that when the stretch is less than 1.3, the NH model and Yeoh model are less accurate and more compliant than the MR model and Ogden model.

It is worth mentioning that the linearized material model could be used when the robot undergoes a small stretch [see Fig. 10(b)], e.g., in [72], where the maximum pressure is 1.38 bar. In such case, the linearized Young's modulus E_l can be considered, e.g., based on the stretch level or parameter identification. To improve the accuracy of kinematics models under a high pressurization level, the chamber stiffening effect is non-negligible [see Figs. 10(a) and (c)]. As reported in this article, choosing hyperelastic models and considering the chamber stiffening can reduce modeling errors.

All soft manipulators in this work feature parallel actuation chambers, which cannot generate torsional torque through internal pressure alone. Torsional motions arise only from external loads. While our model inherently captures the torsional response, we focused on validating bending and elongation behaviors, and these behaviors are the primary deformation modes relevant to our actuator design. As such, torsional motions were not investigated. Exploring torsional responses and potential buckling phenomena remains an important direction for future work, which may involve redesigning the robots to generate torsional motions through internal pressurization.

3) Discussions for Tip Force Generation: The results of the tip force generation correlate with other planar actuators, e.g., the fibre-reinforced bending actuator from [21], and the PneuNets bending actuator from [42], [61]. Specifically, the force-versus-pressure curve indicates a high linear relationship applicable for robots with different dimensions. In general, the length has significantly less influences on the tip force generation than the diameter. Hence, for a specific design, the cross-sectional geometries and selection of materials could be major factors to vary robot's force capability. It is worth noting that the reported modeling errors for the D10 robots are approximately 10%–15% higher than those observed for large-scale robots (e.g., D20 and D25 robots). This increase is primarily attributed to limitations in the force sensor resolution instead of the force model. Specifically, the IIT-FT17 force sensor has a resolution of ± 0.01 N, while the forces measured from the D10 robots are generally below 0.1 N, making the sensor's measurement error more significant. This can be supported by the fact the the model's MAPE in force prediction of is 5.32% for a 11.4 mm robot with an enhanced maximum force of 0.34 N, which is comparable to the modeling performances of larger-scale robots (3.05%–6.23%) reported in Table III. Last, the errors from all the hyperelastic models are around the same level, but the NH model and Yeoh model predict larger forces compared to the MR model and Ogden model. This discrepancy could be attributed to the NH model and Yeoh model exhibiting larger deformations [see Fig. 9(d) and (e)], which results in larger predicted forces.

Moreover, when generating tip blocked tip forces, the chamber pressure value is controlled as invariant. In this case, the pressurized chambers tend to deform instead of contracting lengths. This hypothesis supports the funding that constraining the pressurized chamber length in the model can produce better force prediction results, as shown in Fig. 14. Without considering such length constraints, the predicted force is smaller than the experimentally obtained force. Force model simulations take longer than kinematic simulations due to the added computational complexity of incorporating chamber length and tip position constraints into the optimization formulations. In our case, the computation times for kinematics and force simulations involving eight robots are approximately 0.09–0.15 s and 0.2–1.7 s, respectively. These simulations are executed using MATLAB on a desktop equipped with an Intel i7 processor (3.4 GHz) and 64 GB of RAM.

Table VI compares the accuracy of our static modeling framework against existing approaches focused on static models for pneumatically driven, fibre-reinforced soft actuators of similar

TABLE VI
ACCURACY COMPARISON OF STATIC MODELS FOR PNEUMATICALLY DRIVEN, FIBRE-REINFORCED SOFT ACTUATORS

Reference	Robot Size	Type of Bending	Forward Kinematics modeling Method	Mean Error of Bending Angles	Force modeling Approach	Force modeling Error*	Considering Hyper-elasticity
[21]	Width of 12–24 mm	Uni-directional	FEM	—	FEM	10.3%	Neo-Hookean
[33]	Diameter of 25 mm	Omni-directional	PCC	$12.5^\circ \sim 16.4^\circ$	Not modelled	—	No
[55]	Width of 16 mm	Uni-directional	Beam mechanics	$7.5^\circ \sim 18^\circ$	Beam mechanics	$3\% \sim 10\%$	Power functions
[73]	Diameter of 24 mm	Omni-directional	FEM	$\approx 10^\circ \sim 15^\circ$	Not modelled	—	Neo-Hookean
Our work	Diameter of 10–25 mm	Omni-directional	Cosserat rod model	$< 10^\circ$	Cosserat rod model	$2.7\% \sim 8.5\%$	Various models

* To have a generalized comparison, force modeling accuracy is quantified as the mean force error relative to the maximum observed force.

sizes. Table VI shows that our framework achieves average modeling errors of less than 10° for bending angle prediction and 2.7%–8.5% for force prediction. In comparison, the FEM reported in [21] yields a force prediction error of 10.3%, while the PCC model in [33] shows mean bending angle errors ranging from 12.5° to 16.4°. Sun et al. [55] reported a beam model of uni-directional bending actuators, with bending angle and force prediction errors of 7.5°–18° and 3%–10%, respectively.

4) Discussions for the Applicability of the Framework: The validation of the proposed modeling framework relies on soft robots with reinforced chambers. Please note that the key requirements for applying our method are the robot's geometric dimensions and its material properties, regardless of the specific reinforcement method used. To extend our approach to other types of actuators, such as 3D-printed actuators reinforced through geometric patterns or printing orientations, it is essential to know the actuators' dimensions and identified material's strain-stress behavior. It is noteworthy that our GUI supports user-defined stress–strain functions.

Our approach is capable of handling certain asymmetric geometries, including variations in cross-sectional properties, such as wall thickness and chamber diameter, along the robot's backbone. To capture these variations, the relevant parameters can be expressed as functions of the curve length s, and the constant compliance matrices c_{se} and c_{bt} in (8) become $c_{se}(s)$ and $c_{bt}(s)$, update in each integration step. Similarly, our model can incorporate other chamber shapes, such as semicircular chambers, which requires recalculating the cross-sectional area A and the actuation chamber area A_c, second moments of area I_x and I_y in $c_{se}(s)$ and $c_{bt}(s)$. To ensure modeling accuracy in this case, it is important to account for the potential deformation of noncircular chambers [55]. Incorporating these asymmetric deformations into the modeling framework is an interesting direction for future work.

This work focuses on static models, aiming to provide a practical tool for facilitating robot prototyping. To extend our static modeling framework to include robot dynamics, a set of partial differential equations involving both the spatial curve and time can be derived from the full dynamic Cosserat rod theory [31]. In addition, the dynamics model requires identifying damping coefficients, such as those associated with elongation and bending.

VII. CONCLUSION

In this article, we presented a modeling, design, and evaluation framework for soft manipulators with fibre-reinforced chambers, to systematically describe their key statics performances, i.e., the kinematics and tip force capability. Our framework is capable of coping with the kinematic nonlinearity when the robots undergo larger deformations. Specifically, static models in our framework can be summarized as follows.

1) Analyze robots' forward kinematics and force generation with different design parameters, e.g., cross-sectional geometries, robot lengths, and soft material types.
2) Investigate linearized material or various hyperelastic models (e.g., NH model, MR model, Yeoh model, Ogden model) and consider nonlinear strain-stress deformations resulting from a large longitudinal elongation.
3) Incorporate influences of the chamber stiffening effect resulting from the pressurization.
4) Evaluate key design parameters prior to fabrication, based on the specific application requirements.

We aim for the experiment and simulation results herein to serve as a design reference and the proposed GUI as a toolbox to provide insights for designers, with respect to determining robot design parameters in specific applications (as exemplified in Section V). As such, findings can facilitate robot prototyping and development. In future, we will further investigate control of such fabricated robots. Moreover, we will explore the possibility of generating a unified design, modeling and control framework for multisegment robots.

ACKNOWLEDGMENT

The authors would like to thank the Hamlyn Centre for Robotic Surgery and Prof. Ferdinando Rodriguez y Baena at Imperial College London when revising this work. For any issues related to repository access, please contact the Corresponding or First Author.

REFERENCES

[1] D. Rus and M. T. Tolley, "Design, fabrication and control of soft robots," *Nature*, vol. 521, no. 7553, pp. 467–475, 2015.
[2] M. Manti et al., "A bioinspired soft robotic gripper for adaptable and effective grasping," *Soft Robot.*, vol. 2, no. 3, pp. 107–116, 2015.
[3] Z. Xie et al., "Octopus-inspired sensorized soft arm for environmental interaction," *Sci. Robot.*, vol. 8, no. 84, 2023, Art. no. eadh7852.
[4] X. Dong et al., "Design and control of a musculoskeletal bionic leg with optimized and sensorized soft artificial muscles," *IEEE Trans. Robot.*, vol. 41, pp. 3402–3422, 2025.
[5] S. Rozen-Levy, W. Messner, and B. A. Trimmer, "The design and development of branch bot: A branch-crawling, caterpillar-inspired, soft robot," *Int. J. Robot. Res.*, vol. 40, no. 1, pp. 24–36, 2021.
[6] S. A. Morin et al., "Camouflage and display for soft machines," *Science*, vol. 337, no. 6096, pp. 828–832, 2012.

[7] L. Marechal et al., "Toward a common framework and database of materials for soft robotics," *Soft Robot.*, vol. 8, no. 3, pp. 284–297, 2021.

[8] J. Shi, G. Shi, Y. Wu, and H. A. Wurdemann, "A multi-cavity touch interface for a flexible soft laparoscopy device: Design and evaluation," *IEEE Trans. Med. Robot. Bionics.*, vol. 6, no. 4, pp. 1309–1321, Nov. 2024.

[9] P. Polygerinos et al., "Soft robotics: Review of fluid-driven intrinsically soft devices; manufacturing, sensing, control, and applications in human-robot interaction," *Adv. Eng. Mater.*, vol. 19, no. 12, 2017, Art. no. 1700016.

[10] J. Shi, K. Borvorntanajanya, K. Chen, E. Franco, and F. R. y. Baena, "Design, control and evaluation of a novel soft everting robot for colonoscopy," *IEEE Trans. Robot.*, vol. 41, pp. 4843–4859, 2025.

[11] A. D. Marchese, R. K. Katzschmann, and D. Rus, "A recipe for soft fluidic elastomer robots," *Soft Robot.*, vol. 2, no. 1, pp. 7–25, 2015.

[12] R. V. Martinez et al., "Robotic tentacles with three-dimensional mobility based on flexible elastomers," *Adv. Mater.*, vol. 25, no. 2, pp. 205–212, 2013.

[13] L. Lindenroth, S. Bano, A. Stilli, J. G. Manjaly, and D. Stoyanov, "A fluidic soft robot for needle guidance and motion compensation in intratympanic steroid injections," *IEEE Robot. Autom. Lett.*, vol. 6, no. 2, pp. 871–878, Apr. 2021.

[14] L. Manfredi, E. Capoccia, G. Ciuti, and A. Cuschieri, "A soft pneumatic inchworm double balloon (SPID) for colonoscopy," *Sci. Rep.*, vol. 9, no. 1, pp. 1–9, 2019.

[15] J. Fraś et al., "New STIFF-FLOP module construction idea for improved actuation and sensing," in *Proc. IEEE Int. Conf. Robot. Autom.*, 2015, pp. 2901–2906.

[16] A. B. Dawood et al., "Fusing dexterity and perception for soft robot-assisted minimally invasive surgery: What we learnt from STIFF-FLOP," *Appl. Sci.*, vol. 11, no. 14, 2021, Art. no. 6586.

[17] K. Suzumori, S. Iikura, and H. Tanaka, "Applying a flexible microactuator to robotic mechanisms," *IEEE Control Syst. Mag.*, vol. 12, no. 1, pp. 21–27, Feb. 1992.

[18] T. Ranzani, M. Cianchetti, G. Gerboni, I. D. Falco, and A. Menciassi, "A soft modular manipulator for minimally invasive surgery: Design and characterization of a single module," *IEEE Trans. Robot.*, vol. 32, no. 1, pp. 187–200, Feb. 2016.

[19] Y. Sun, S. Song, X. Liang, and H. Ren, "A miniature soft robotic manipulator based on novel fabrication methods," *IEEE Robot. Autom. Lett.*, vol. 1, no. 2, pp. 617–623, Jul. 2016.

[20] J. Fras, Y. Noh, H. Wurdemann, and K. Althoefer, "Soft fluidic rotary actuator with improved actuation properties," in *Proc. IEEE/RSJ Int. Conf. Intell. Robots Syst.*, 2017, pp. 5610–5615.

[21] P. Polygerinos et al., "Modeling of soft fiber-reinforced bending actuators," *IEEE Trans. Robot.*, vol. 31, no. 3, pp. 778–789, Jun. 2015.

[22] J. Shi, W. Gaozhang, and H. A. Wurdemann, "Design and characterisation of cross-sectional geometries for soft robotic manipulators with fibre-reinforced chambers," in *Proc. IEEE Int. Conf. Soft Robot.*, 2022, pp. 125–131.

[23] Z. Gong et al., "A soft manipulator for efficient delicate grasping in shallow water: Modeling, control, and real-world experiments," *Int. J. Robot. Res.*, vol. 40, no. 1, pp. 449–469, 2021.

[24] Y. Cui et al., "Design and implementation of an underactuated gripper with enhanced shape adaptability and lateral stiffness through semi-active multi-degree-of-freedom endoskeletons," *Int. J. Robot. Res.*, vol. 43, no. 6, pp. 873–896, 2024.

[25] H. Abidi et al., "Highly dexterous 2-module soft robot for intra-organ navigation in minimally invasive surgery," *Int. J. Med. Robot. Comput. Assist. Surg.*, vol. 14, no. 1, 2018, Art. no. e1875.

[26] C. Della Santina, C. Duriez, and D. Rus, "Model-based control of soft robots: A survey of the state of the art and open challenges," *IEEE Control Syst. Mag.*, vol. 43, no. 3, pp. 30–65, Jun. 2023.

[27] C. Duriez, "Control of elastic soft robots based on real-time finite element method," in *Proc. IEEE Int. Conf. Robot. Autom.*, 2013, pp. 3982–3987.

[28] P. Chaillou, J. Shi, A. Kruszewski, I. Fournier, H. A. Wurdemann, and C. Duriez, "Reduced finite element modelling and closed-loop control of pneumatic-driven soft continuum robots," in *Proc. IEEE Int. Conf. Soft Robot.*, 2023, pp. 1–8.

[29] R. J. Webster III and B. A. Jones, "Design and kinematic modeling of constant curvature continuum robots: A review," *Int. J. Robot. Res.*, vol. 29, no. 13, pp. 1661–1683, 2010.

[30] C. Della Santina, R. K. Katzschmann, A. Bicchi, and D. Rus, "Model-based dynamic feedback control of a planar soft robot: Trajectory tracking and interaction with the environment," *Int. J. Robot. Res.*, vol. 39, no. 4, pp. 490–513, 2020.

[31] J. Till, V. Aloi, and C. Rucker, "Real-time dynamics of soft and continuum robots based on Cosserat rod models," *Int. J. Robot. Res.*, vol. 38, no. 6, pp. 723–746, 2019.

[32] J. Sun and J. Zhao, "Physics-based modeling of twisted-and-coiled actuators using Cosserat rod theory," *IEEE Trans. Robot.*, vol. 38, no. 2, pp. 779–796, Apr. 2022.

[33] J. Shi et al., "Stiffness modelling and analysis of soft fluidic-driven robots using Lie theory," *Int. J. Robot. Res.*, vol. 43, no. 3, pp. 354–384, 2024.

[34] F. Renda, F. Boyer, J. Dias, and L. Seneviratne, "Discrete Cosserat approach for multisection soft manipulator dynamics," *IEEE Trans. Robot.*, vol. 34, no. 6, pp. 1518–1533, Dec. 2018.

[35] H. Li, L. Xun, and G. Zheng, "Piecewise linear strain Cosserat model for soft slender manipulator," *IEEE Trans. Robot.*, vol. 39, no. 3, pp. 2342–2359, Jun. 2023.

[36] S. Lilge, T. D. Barfoot, and J. Burgner-Kahrs, "Continuum robot state estimation using Gaussian process regression on SE(3)," *Int. J. Robot. Res.*, vol. 41, no. 13/14, pp. 1099–1120, 2022.

[37] I. Singh, Y. Amara, A. Melingui, P. Mani Pathak, and R. Merzouki, "Modeling of continuum manipulators using Pythagorean hodograph curves," *Soft Robot.*, vol. 5, no. 4, pp. 425–442, 2018.

[38] G. Thuruthel et al., "Learning closed loop kinematic controllers for continuum manipulators in unstructured environments," *Soft Robot.*, vol. 4, no. 3, pp. 285–296, 2017.

[39] C.-P. Chou and B. Hannaford, "Measurement and modeling of McKibben pneumatic artificial muscles," *IEEE Robot. Autom. Lett.*, vol. 12, no. 1, pp. 90–102, Feb. 1996.

[40] F. Connolly, P. Polygerinos, C. J. Walsh, and K. Bertoldi, "Mechanical programming of soft actuators by varying fiber angle," *Soft Robot.*, vol. 2, no. 1, pp. 26–32, 2015.

[41] F. Connolly, C. J. Walsh, and K. Bertoldi, "Automatic design of fiber-reinforced soft actuators for trajectory matching," *Proc. Nat. Acad. Sci.*, vol. 114, no. 1, pp. 51–56, 2017.

[42] A. S. Camp, E. M. Chapman, and P. Jaramillo Cienfuegos, "Modeling and analysis of hydraulic piston actuation of mckibben fluidic artificial muscles for hand rehabilitation," *Int. J. Robot. Res.*, vol. 40, no. 1, pp. 136–147, 2021.

[43] S. H. Sadati et al., "TMTDyn: A MATLAB package for modeling and control of hybrid rigid–continuum robots based on discretized lumped systems and reduced-order models," *Int. J. Robot. Res.*, vol. 40, no. 1, pp. 296–347, 2021.

[44] F. Renda, M. Cianchetti, H. Abidi, J. Dias, and L. Seneviratne, "Screw-based modeling of soft manipulators with tendon and fluidic actuation," *J. Mech. Robot.*, vol. 9, no. 4, 2017, Art. no. 041012.

[45] X. Huang, X. Zhu, and G. Gu, "Kinematic modeling and characterization of soft parallel robots," *IEEE Trans. Robot.*, vol. 38, no. 6, pp. 3792–3806, Dec. 2022.

[46] H. Al-Fahaam, S. Nefti-Meziani, T. Theodoridis, and S. Davis, "The design and mathematical model of a novel variable stiffness extensor-contractor pneumatic artificial muscle," *Soft Robot.*, vol. 5, no. 5, pp. 576–591, 2018.

[47] C. Wielgosz et al., "Bending and buckling of inflatable beams: Some new theoretical results," *Thin-Walled Struct.*, vol. 43, no. 8, pp. 1166–1187, 2005.

[48] D. P. Holland et al., "The soft robotics toolkit: Strategies for overcoming obstacles to the wide dissemination of soft-robotic hardware," *IEEE Robot. Autom. Mag.*, vol. 24, no. 1, pp. 57–64, Mar. 2017.

[49] S. Joshi and J. Paik, "Multi-DoF force characterization of soft actuators," *IEEE Robot. Autom. Lett.*, vol. 4, no. 4, pp. 3679–3686, Oct. 2019.

[50] A. T. Mathew, I. M. B. Hmida, C. Armanini, F. Boyer, and F. Renda, "SoRoSim: A MATLAB toolbox for hybrid rigid-soft robots based on the geometric variable-strain approach," *IEEE Robot. Autom. Mag.*, vol. 30, no. 3, pp. 106–122, Sep. 2023.

[51] B. J. Caasenbrood, A. Y. Pogromsky, and H. Nijmeijer, "Sorotoki: A Matlab toolkit for design, modeling, and control of soft robots," *IEEE Access*, vol. 12, pp. 17604–17638, 2024.

[52] Y. Yao, L. He, and P. Maiolino, "SPADA: A toolbox of designing soft pneumatic actuators for shape matching based on surrogate modeling," *Robot. Rep*, vol. 2, no. 1, pp. 1–14, 2024.

[53] P. Moseley et al., "Modeling, design, and development of soft pneumatic actuators with finite element method," *Adv. Eng. Mater.*, vol. 18, no. 6, pp. 978–988, 2016.

[54] F. Renda et al., "A unified multi-soft-body dynamic model for underwater soft robots," *Int. J. Robot. Res.*, vol. 37, no. 6, pp. 648–666, 2018.

[55] Y. Sun, H. Feng, I. R. Manchester, R. C. H. Yeow, and P. Qi, "Static modeling of the fiber-reinforced soft pneumatic actuators including inner compression: Bending in free space, block force, and deflection upon block force," *Soft Robot.*, vol. 9, no. 3, pp. 451–472, 2022.